gti

Reduced Mandated Inspection by Remote Field Eddy Current Inspection of Unpiggable Pipelines

Technical Final Report

Reporting Period Start Date: October 1, 2005
Reporting Period End Date: September 30, 2006

GTI Project Manager: Albert Teitsma
GTI Principal Investigator: Julie Maupin

October 2006

DE-FC26-04NT42266

Prepared by:
Gas Technology Institute
1700 S. Mount Prospect Road
Des Plaines, Illinois 60018

DISCLAIMER

TABLE OF CONTENTS

EXECUTIVE SUMMARY

The Remote Field Eddy Current (RFEC) technique is ideal for inspecting unpiggable pipelines because all of its components can be made much smaller than the diameter of the pipe to be inspected. For this reason, RFEC was chosen as a technology for unpiggable pipeline inspections by DOE-NETL with the support of OTD and PRCI, to be integrated with platforms selected by DOE-NETL. As part of the project, the RFEC laboratory facilities were upgraded and data collection was made nearly autonomous. The resulting improved data collection speeds allowed GTI to test more variables to improve the performance of the combined RFEC and platform technologies. Tests were conducted on 6", 8", and 12" seamless and seam-welded pipes. Testing on the 6" pipes included using seven exciter coils, each of different geometry with an initial focus on preparing the technology for use on an autonomous robotic platform with limited battery capacity. Reductions in power consumption proved successful. Tests with metal components similar to the Explorer II modules were performed to check for interference with the electromagnetic fields. The results of these tests indicated RFEC would be able to produce quality inspections while on the robot. Mechanical constraints imposed by the platform, power requirements, control and communication protocols, and potential busses and connectors were addressed. Much work went into sensor module design including the mechanics and electronic diagrams and schematics. GTI participated in two Technology Demonstrations for inspection technologies held at Battelle Laboratories. GTI showed excellent detection and sizing abilities for natural corrosion. Following the demonstration, module building commenced but was stopped when funding reductions did not permit continued development for the selected robotic platform. Conference calls were held between GTI and its sponsors to resolve the issue of how to proceed with reduced funding. The project was rescoped for 10-16" pipes with the intent of looking at lower cost, easier to implement, tethered platform applications. OTD ended its sponsorship.

THE REMOTE FIELD EDDY CURRENT TECHNIQUE

The remote field eddy current (RFEC) technique was patented by W. R. McLean (US Patent 2,573,799, "Apparatus for Magnetically Measuring Thickness of Ferrous Pipe", Nov.6, 1951) and first developed by Tom Schmidt at Shell for down hole inspection (Schmidt, T. R., "The Casing Instrument Tool- …", Corrosion, pp 81-85, July 1961). The RFEC technology has many advantages including:

- A simple exciter coil that can be less than one-third of the pipe diameter. The exciter coil does not need to be close to the wall. [3 pt spacing]
- Simple and small (millimeter to centimeter diameter) sensor coils that do not need to contact the wall. Thus, the diameter of the coil array can be easily adjusted to match the pipe diameter yet pass through a small opening.
- Sensor coils close to the pipe wall provide sensitivity and accuracy comparable to standard MFL inspection tools. General pipe corrosion of 10% of the wall thickness or less is detected and measured with commercial units.
- Sensor lift-off, up to 0.75 inch can be automatically compensated for, though sensitivity and resolution will be compromised.

The technique is commercially viable for inspecting boiler tubes and pipe diameters up to 8 inches for several hundred feet. Russell Technologies developed an 18 inch device that can inspect production wells for several thousand feet. However, none of the current versions are collapsible to one-third of the pipe diameter or less, nor can any handle short-radius elbows and other obstacles. To adapt the technique for this application will require investigating variations such as transmitter coil angle and methods for either reducing the variations or sensitivity to them. Larger diameters should not be a problem since specialized tools can inspect the steel reinforcing of 12 foot diameter concrete water mains (Atherton, D. L., US patent 6,127,823, "Electromagnetic Method for Non-Destructive Testing of Prestressed Concrete Pipes for Broken Prestressed Wires", Oct. 3, 2000).
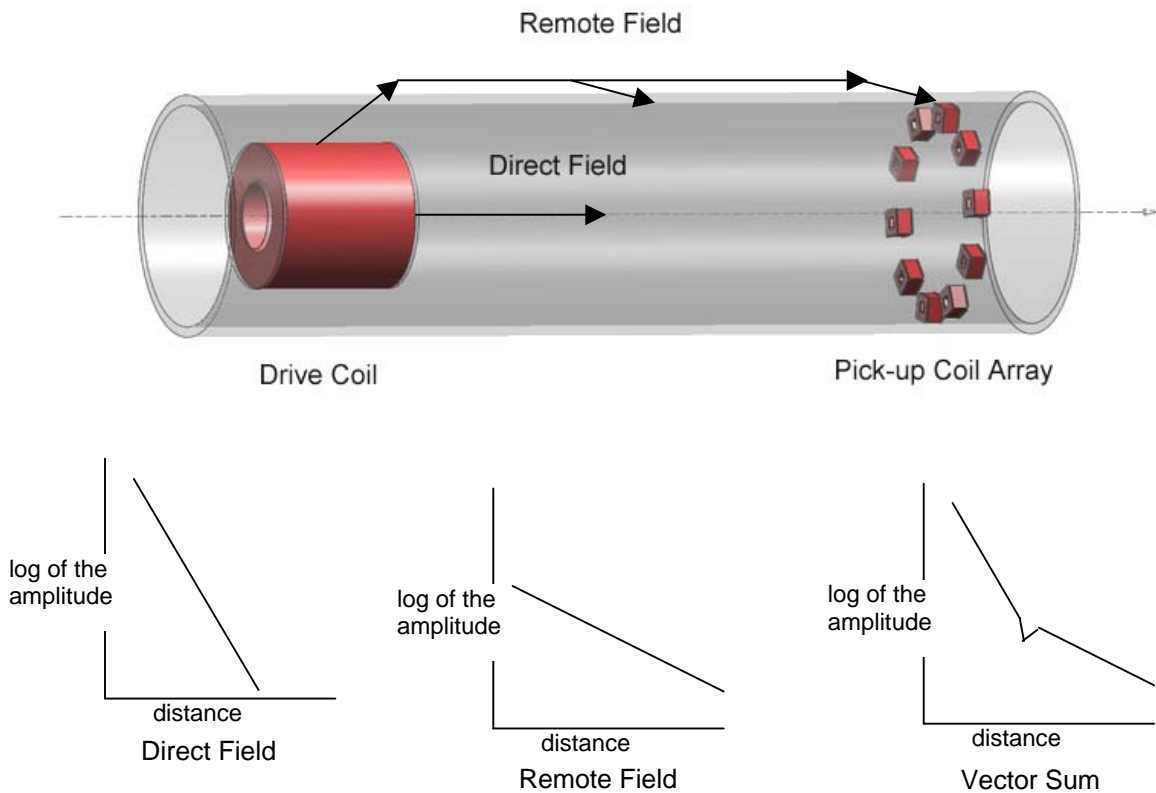
Figure 1: Variation of the amplitude of propagating fields with distance along a pipe.

Figure 1 shows the basics of the remote field eddy current (RFEC) method. The exciter coil sends 20 Hz to 200 Hz electromagnetic waves propagating down the pipe and through the pipe wall. The electromagnetic waves traveling inside the pipe (direct field) are highly attenuated because they are well below the cutoff frequency for propagation – for which frequencies need to be in the gigahertz range - in a wave-guide. As far as the electromagnetic waves are concerned, a pipeline is nothing more than a wave-guide. Approximately two pipe diameters from the source coil, these 'direct' waves all but vanish. Meanwhile, the waves that have penetrated the wall (remote field) can penetrate back into the pipe as well. At about two pipe diameters from the exciter coil and beyond, these waves swamp the direct field waves attempting to propagate down the bore of the pipe and, therefore, can be detected and measured. This is the reason for the term "remote field eddy currents" (as opposed to the near or direct field currents from waves propagating down the bore of the pipe). This is exactly

what is needed. Any pipeline flaws such as metal loss from corrosion or other causes that affect the propagation of these RFECs back into the pipe alter the detected signal so that the flaws may be detected and measured by the sensing coils.
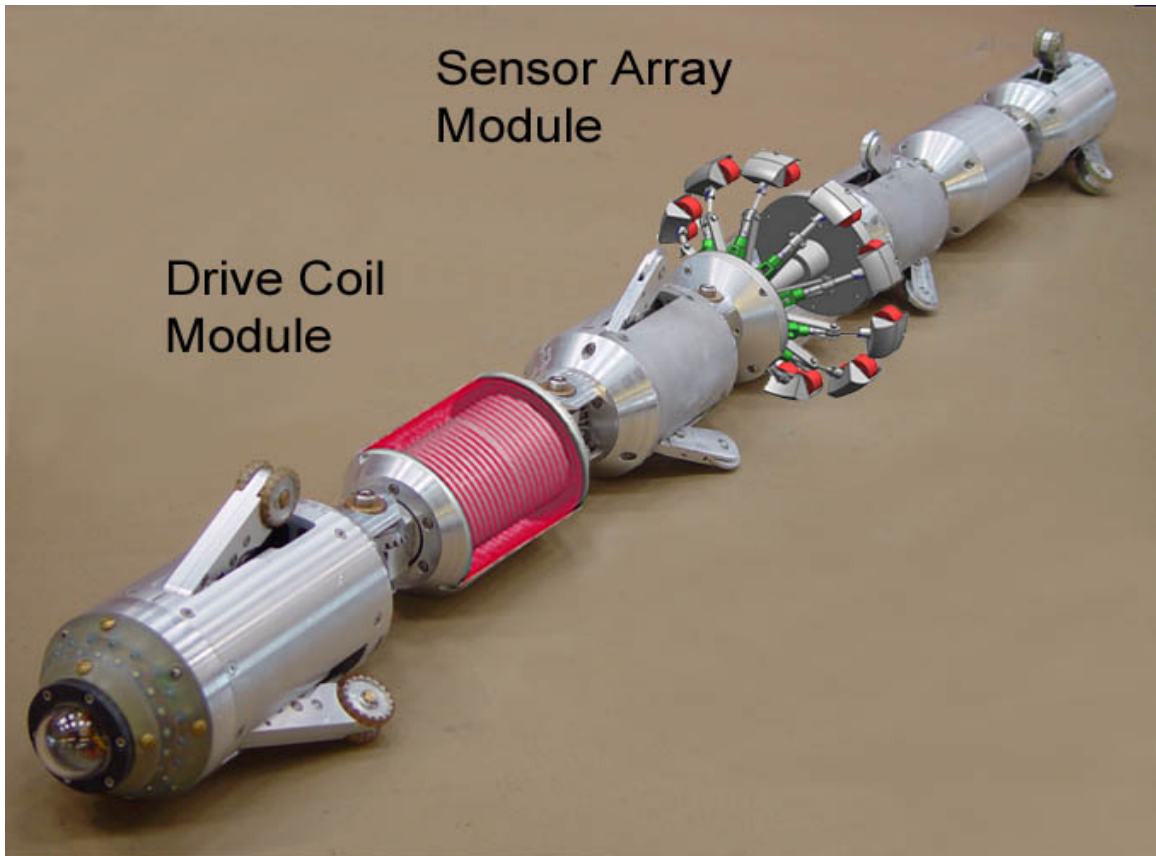
Figure 2: A simulated drawing of the RFEC technology integrated with Explorer.

The RFEC frequencies need to be low since higher frequencies will not penetrate ferromagnetic conductors such as pipeline steel. Methods to increase penetration by lowering the magnetic permeability by magnetizing the pipe may not work well for unpiggable pipelines for the some of the same reasons that MFL inspection will not work well. The one disadvantage of the technique will therefore be slow inspection speeds. Other than that, the RFEC technique is the ideal in-line inspection technology for inspecting "unpiggable" pipelines. The transmitter and sensors can be designed to fit through anything that robots or any design of pig driving cups can pass through. Figure 2 shows a conceptual design for a proposed inspection device using Explorer II to propel the tool

through a distribution main. The exciter coil can be much smaller than the pipeline diameter and mounted on a short module. Power and electronic modules, including possibly a recharging module, can be mounted ahead and between the transmitter and the sensors with additional modules, if needed, following behind these. Modules at each end of the RFEC in-line inspection tool can move the tool in either direction.

PROJECT OBJECTIVES

The primary objective of this project was to develop Remote Field Eddy Current methods for inspecting unpiggable pipelines. The first two research tasks were writing a Research Management Plan and a Technology Status Assessment Report. Task 3 called for proof of the feasibility of RFEC as an unpiggable pipeline inspection technology. Additional objectives included Product Definition, Electronics and Operational Prototype Development.

NON EXPERIMENTAL

GTI completed Task 1, the Research Management Plan, which detailed the work to be performed under this project. GTI also completed the technology Assessment Report that described both the status of the RFEC technology and where it fit within available technologies for enhancing pipeline reliability. The feasibility of inspecting transmission pipelines using the RFEC technique was proven early in the project. We proved the technique's ability to use small components, thereby confirming it suitable for unpiggable pipeline inspection.

The scope of work under this project included collaborative work with the DOE-NETL selected platform designers. For much of the project, the Explorer II robot at Carnegie Mellon University (CMU) was the target. This work consisted of sensor/platform definition, where we drafted requirements of our sensor, created three module designs using 3D modeling software for the mid phase design review, and completed one design for the final design review. The final design included electronic schematics and specifications as well as a complete bill of materials. The final design review was held at CMU in December, 2005, at which time, we had also completed our set of Sensor Module Commands for facilitation of information exchange over the Explorer II CANbus.

When GTI received notice that its sensors would not be integrated with Explorer II due to funding cuts at DOE, the project was rescoped slightly to address 10-16" diameter pipes. The design team updated the rotating type design for the larger scale. It increased the number of sensors and improved the rotation mechanism and sensor arms. This latest design was built and is discussed later in this report.

Additionally, GTI provided monthly reports and annual project update presentations.

EXPERIMENTAL
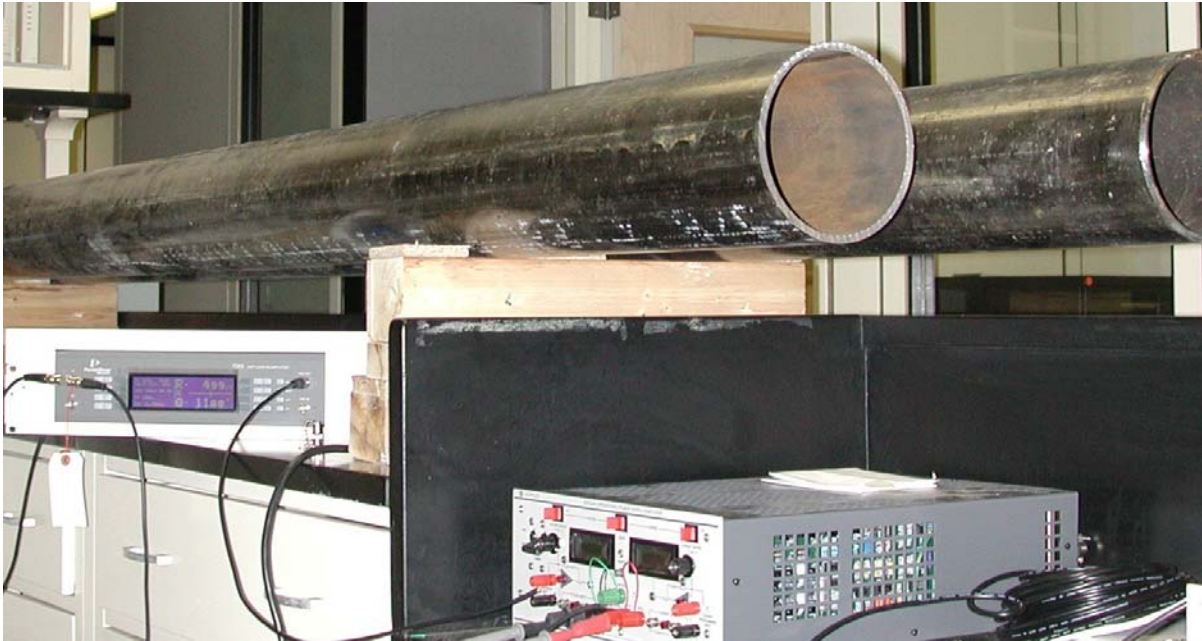
Figure 3: RFEC laboratory setup.

Figure 3 shows the laboratory setup for performing the majority of the RFEC research tasks. We machined defects sets into two 10' sections of 6" diameter pipe. One pipe is seamless, the other is seam welded. For each pipe a Kepco BOP, bipolar operational power supply, shown on the right, drives the exciter coil and a PerkinElmer lock-in amplifier, shown on the left, filters and amplifies the signal received by the sensing coil.

We started with an exciter coil made of 1000 turns of #29 copper wire wound 2" wide on a 1 ½" diameter spool. Electromagnetic waves for the remote field were generated by driving the coil at 8.6 V rms and 0.2 A rms by the BOP. The sensing coil was made of 20,000 turns of #46 copper wire wound on a 3/8" wide, ¾" diameter bobbin. The output of the sensing coil is filtered and amplified by the lock-in amplifier. The lock-in amplifier rejects all frequencies except that of its internal oscillator. The internal oscillator of the lock-in amplifier provides the signal that is amplified by the BOP to drive the exciter coil.

In 2004, we performed RFEC testing on 12" seamless and seam-welded pipes. This testing was initially started in preparation for the DOE-NETL technology demonstration held at Battelle Laboratories in Ohio. We continued to work with the 12" pipes for a month or so after returning to GTI.

Late in 2005, we rebuilt our laboratory vehicle to accommodate the sensors through an 8" diameter pipe in preparation for a second demonstration at Battelle in January 2006. We achieved good results using the same exciter and sensing coils as we had been using in the 6" pipe, further illustrating the ability to use RFEC coils that are much smaller than the pipe diameter.

ELECTRONICS and DATA ACQUISITION IMPROVEMENTS

We built a 16 channel multiplexer for use on the 6" pipes in the laboratory. In order to collect data for 16 sensor coils, we updated our LabVIEW data acquisition program to step through and record data from all 16 channels. The LabVIEW program also controlled the location of the sensors and recorded position data from the odometer at data acquisition locations.

Using the multiplexer board and LabVIEW significantly improved collection speeds. Manually, it would take close to two hours to inspect a single defect. Using the new autonomous system, all 13 defects along a 10' section of pipe could be inspected in an hour and a half without a researcher present. Further improvements in inspection speeds were seen when GTI purchased and employed a Ferroscope electronics circuit and software from Russell Technologies, Inc. This is a much more sophisticated system as Russell has years of experience using the RFEC technique to inspect boiler tubes. The collection speeds for this setup are about 3 minutes for a 10' length of pipe.

LAB APPARATUS

We made improvements in the 6" vehicle. The original vehicle had one coil mounted on an arm. To be able to mount multiple coils, we drilled equally spaced holes into a 6" disc and mounted three sets of 5 coils each at 120° locations. This new vehicle allowed us to scan all the defect sets at the same time using the BOP and lock-in setup. We also installed a motor-encoder mechanism to automate the data collection. In addition, a self-righting mechanism was put in place to prevent major rotations of the vehicle. This eliminates the need to "uncurl" the data during analysis.

We attached a 4' section of 6" PVC pipe to the starting end of the seamless pipe. The PVC pipe has large windows cut out of it to facilitate changing components on the vehicle. It also allows us to start taking measurements from the zero mark rather than starting at 33". This lets us inspect the defects located at 24" and 30" without pulling the RFEC vehicle through from the other end.

In addition to the 6" vehicle, we built vehicles for 8" and 12" inspections. GTI also built an apparatus to transport the Russell Equipment through 6" and 8" pipe. The Russell equipment was demonstrated at the benchmarking test in 2006.

GEOMETRIC & SYSTEM STUDIES

We studied drive and sensor coils separation distance as a function of frequency. We obtained understandable results at frequencies up to about 2 KHz. We also studied defect detection at a set frequency as a function of sensor orientation to pipe axis. The results of these studies are discussed in the results section of this report. We wound and tested multiple exciter coils in both the 12" and 6" pipes. These studies enabled us to reduce power consumption, which is important for a tetherless robot, which has limited power.

DRIVE COIL DESIGN OPTIMIZATION

The 10"–16" RFEC design is for a tethered system, which does not have the power restrictions of a robotic system. In that case, there is not the need to balance power consumption versus defect detectability and the coil design can be optimized as a function of frequency to maximize the magnetic dipole moment. The frequency itself is selected primarily based on the magnetic permeability and wall thickness of the pipe, but it can be adjusted for inspection speed – higher frequency for higher speed – and/or transition zone location – the location increases in distance from the drive coil with increasing frequency. A conservative limit of about half an ampere per volt was set for the drive coil i.e. if

the power supply for it put out 10 V, then the maximum current in the drive coil would be about 5A.

The function of the drive coil is to generate a dipole moment given by

$$M=\mu_r\mu_0 NAi \qquad (1)$$

where M is the magnetic moment, μ_0 is the permeability of free space, μ_r is the relative magnetic permeability, N is the number of turns of wire on the coil, A is the area of the coil, and i is alternating current.

$$i=v/Z \qquad (2)$$

where v is the alternating voltage, and Z is the complex impedance.

$$Z=R+j\omega L \qquad (3)$$

where R is the resistance, j is the square root of –1, and L is the inductance. For a coil the resistance is given by the resistance per unit length times the wire length. The resistance per unit length is obtained from the resistivity and the wire diameter, which is determined by the wire gauge.

For a practical coil, the inductance is approximated by

$$L=\mu_r \frac{0.8r^2N^2}{6r+9l+10d} \qquad (4)$$

Where u_r is the relative magnetic permeability, r is the mean radius of the coil, l is the length of the coil and d is the coil thickness, with the dimensions in inches.

These equations along with those relating gauge to wire diameter, and resistance per unit length to resistivity, were programmed into a Matlab program. Matlab was used because it is matrix based and thus handles arrays of values for the variables such as permeability, and wire diameters as simple variables. The dipole moment was then calculated as a function of wire gauge, core permeability and number of wire turns in the coil. The calculations were compared to measured results.

The calculated results are shown in Figure 4 as a function of the logarithm of the number of turns and the relative permeability. For convenience, the result plotted is the frequency times the moment, since that is what the sensing coils measure. As the frequency and the gauge increase the transition
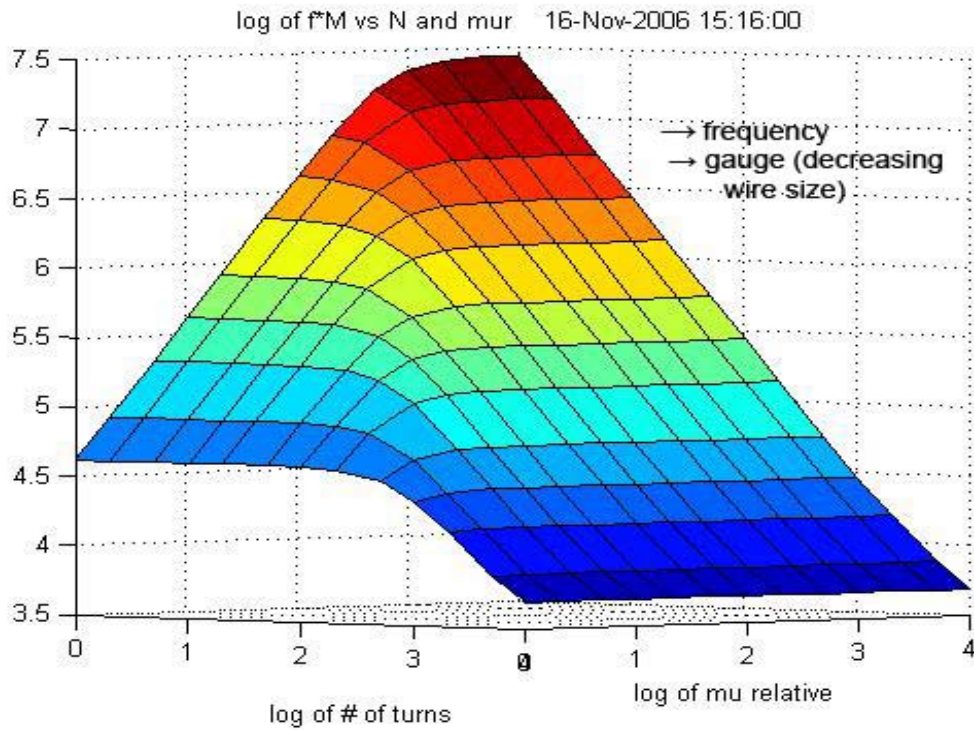
Figure 4: The logarithm of the dipole moment as a function of the number of turns and the relative permeability.

from an impedance dominated by resistance to that dominated by inductance shifts to the right. Note that increasing wire gauge corresponds to decreasing wire diameter. The figure shows the results for a 3.5" diameter coil, which is suitable for most 10" to 16" unpiggable pipe. For 10" and 12" pipe with plug valves, or any pipe with severe bore restrictions, smaller diameter coils can be used. The increased allowable power consumption for a tethered system will compensate for the decrease in coil diameter.

The calculations assume one coil per module. The figure shows that for a fixed relative permeability the measured field increases with a decreasing number of turns until the current through the drive coil is resistance limited. The output is then constant, but the signal can be increased by increasing the number of coils

on the drive module until the current limit of the power supply is reached. Increasing the permeability of the drive coil increases the signal until the current is limited by the inductance.

Comparison to measured results agreed qualitatively with the calculations, provided relative permeability values of around 10 are assumed.

FINITE ELEMENT ANALYSIS CALCULATIONS

Finite Element Analysis (FEA) can provide insight into how the electromagnetic energy propagates through the bore or the pipe and how it propagates outside the pipe wall and then returns to the inside of the pipe where it can be detected by the sensing coils. It can quickly show how obstructions affect the electromagnetic waves, and in detailed 3D calculation show the how defects affect the electromagnetic radiation to generate the defect signals. One important advantage of such calculations is the ability to see what is happening to the electromagnetic fields in the pipe wall, a region not readily accessible experimentally. GTI used the COMSOLAB multi-physics software package to model a mockup of the RFEC inspection system developed for inspecting 6" to 8" pipe.

Figure 5 shows the magnetic flux density lines for a model of the 6" diameter by 0.25" wall thickness 10' long seamless steel pipe used in the NDE laboratory for the RFEC experiments. Axial symmetry reduces the calculation to a 2D calculation, while reflection symmetries reduce the calculation to a one quarter model. The top view shows the full model. The electrical insulation boundary conditions at the top and sides ensure that the magnetic flux meets the boundaries at right angles there, as would be expected for flux lines far from the source. There are places where it is obviously not quite correct, but these are far enough from the regions of interest to not affect the calculations there. The drive is a 2" diameter, 2" long coil at the right bottom corner (not visible), with 4000 ampere-turns of drive current. The frequency for the calculation was 50 Hz. The pipe permeability was set at 100, which may be low, but the results seem reasonable. The bottom of the model has the axial symmetry boundary condition.

The bottom of Figure 5 is an enlargement showing the flux density in and around the 6" pipe and shows the fields at the coil and the pipe end effects.
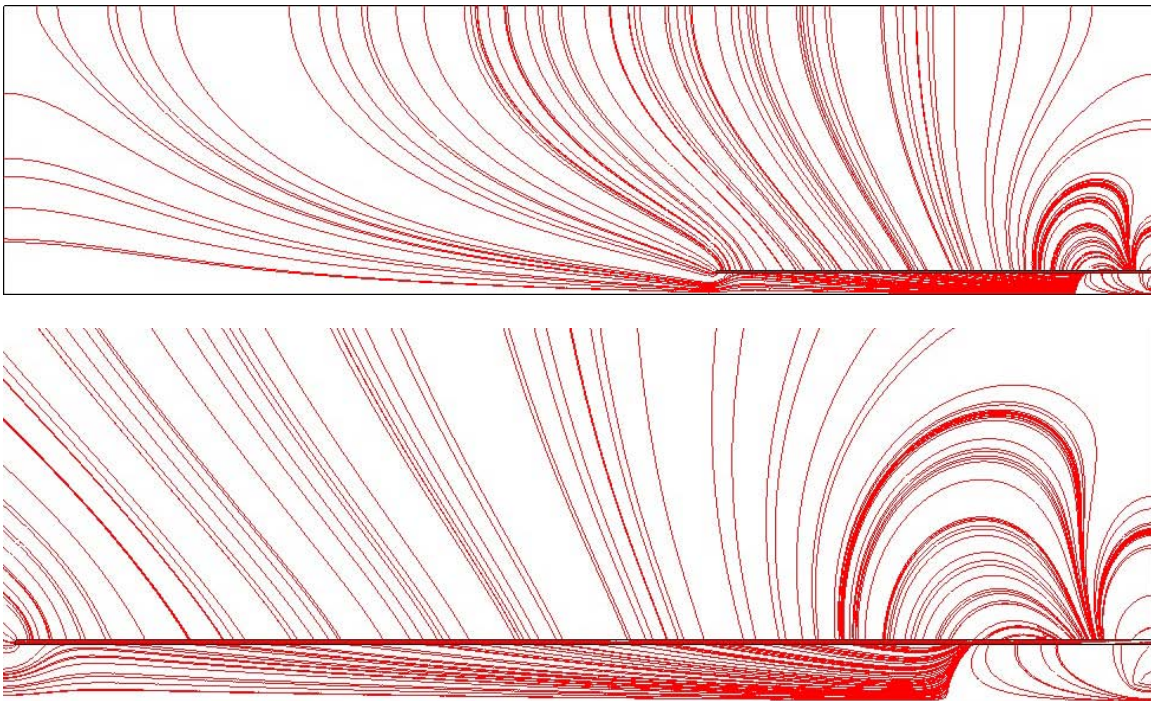
Figure 5: The FEA model of the 6" x 0.25" seamless pipe, showing lines of magnetic flux density.

We used the calculations to investigate the effects of robot modules on the propagation of the electromagnetic fields. Experimental results showed that these modules would improve the RFEC measurements and the calculation verified that as is shown in Figure 6. The top of the figure shows the field near the drive coil and a pullout along the axis of the 6" pipe. The result compares favorably with the measurements shown in figures 11 and 13, which show the transition region at 8" while the calculations show it at 0.28 m, or about 11". The bottom of Figure 6 shows the effect of inserting an empty aluminum robot module, 4" in diameter by 6" long, and with 0.25" wall thickness. The magnetic flux loop shown through the module wall shows the strong eddy currents set up in the module. Those eddy currents are generated by the direct field trying to propagate down the bore of the tube, greatly reducing it. As a result, the remote field becomes larger than the direct field sooner, and the transition region moves

closer to the drive module as shown by the pullout curve, where the transition region has moved inward to 0.22 m, or about 8.5" from 11".
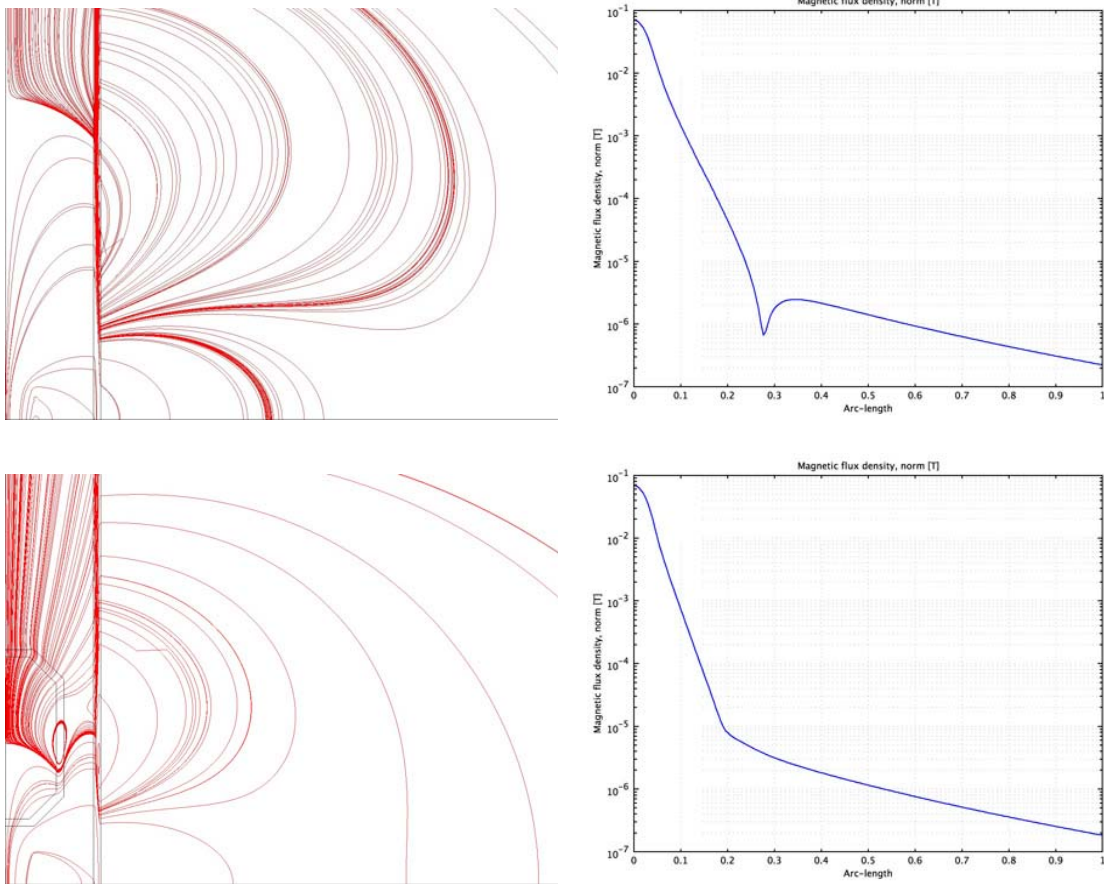
Figure 6: Robot modules attenuate the direct field more rapidly.

The FEA calculations also showed that large values for the relative permeability, and high frequencies i.e. large reductions in the skin depth, move the transition region further away from the drive coil. In one extreme calculation the zone was located at 0.5 m, or about 20". The planned 3D defect modeling was not completed because of funding reductions.

RESULTS AND DISCUSSION

WORK PERFORMED ON 6" PIPE
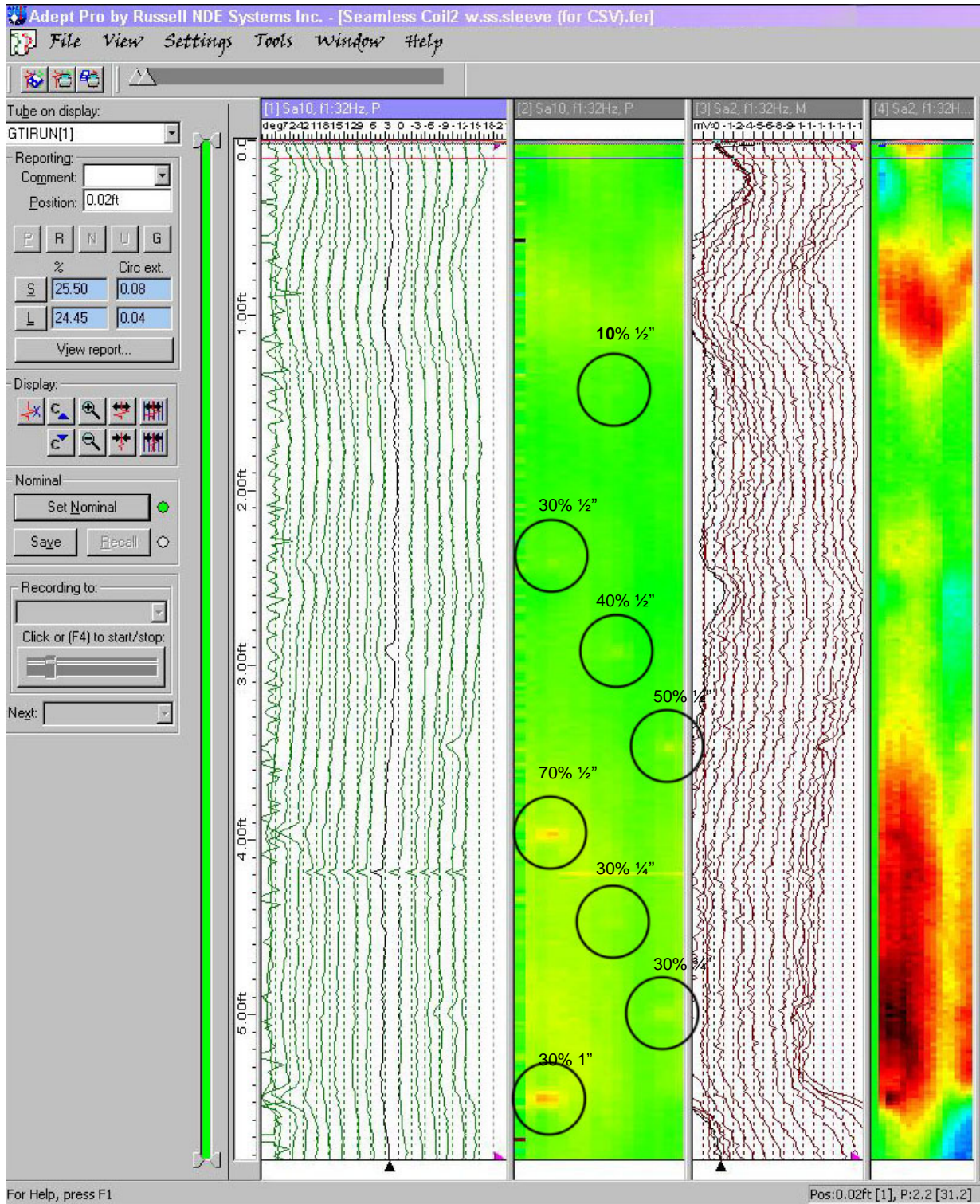
Figure 7: Screen shot of 6" seamless pipe scan from Adept Pro Software.

Figure 7 is a scan of the entire 6" seamless pipe. During this test, a stainless steel sleeve, was placed between the exciter and sensor coils. We were testing the effect of metal components on detection results since robotic components are metallic and size restrictions require at least one module between the drive coil and the sensors. Our concern is that the metal could disrupt the electromagnetic fields and produce poor results. In actuality, we obtained better results with the sleeve inserted. This scan covered 10 defects. Eight of them are identifiable in the strip chart to the left of the screenshot. The two defects that did not show in the data were a 5% ½" and a 30% ¼" defect. We suspect the 30% defect was not detected because we scan in ¼" steps. It is likely that we stepped right over that defect. The results seem to be very promising as the 10% ½" defect was found. We repeated this test with a chunk of aluminum of 3" diameter and 3" in length between the exciter coil and sensing coils. The results were slightly noisier but there was no apparent drop in the amplitude of the signal. The smallest defect detected in this run was a 30% ½" round.

Additional testing was performed on a rusting 6" lined Cast Iron pipe. The RFEC technique has a broad range of applications in conducting and ferromagnetic materials and we took advantage of an opportunity that came up to demonstrate its capabilities. The technique was able to measure the remaining wall thickness through the liner. Despite the Cast Iron appearing to have some remaining wall thickness, the RFEC methods showed existing through wall graphitization, which shows in Figure 8 as dark red.

Pos:1.65s [33], P:0.0 [107.7]
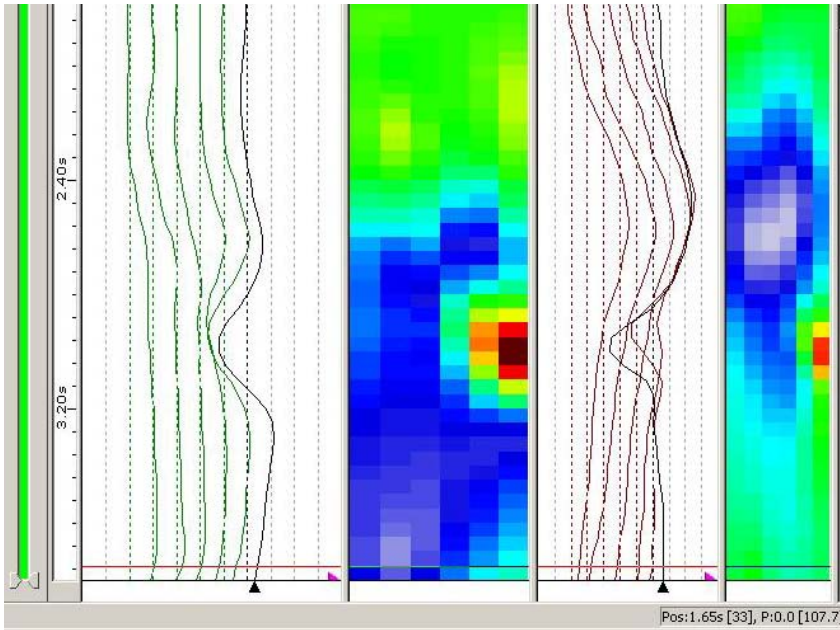
Figure 8: Screen shot of 6" lined Cast Iron.

DIFFERENTIAL COIL TESTING

After completing the above testing with metal components, we performed a study of differential coils. Our differential coils consisted of two identical coils mounted close to each other on the same axis and were operated with each coil 180° out of phase with the other's current. Data analysis included taking the absolute measurement of each coil then subtracting them to get the differential. Results of scanning the pipe along all three defect lines of the 6" seamless pipe are shown in Figure 9. The absolute measurements are plotted in red and orange and the differential measurement is plotted in yellow. The bright red vertical lines represent defect locations along the length of the pipe. The defects measured absolutely are indicated by significant increases in amplitude. A sharp drop followed by a sharp increase in amplitude indicates differential defects. These can be seen in Figure 9. The most obvious is the 80% deep defect located around 78" on Line 1. Because of the length of the RFEC vehicle, we were unable to scan the entire pipe in one pass. For each coil tested, we turned the vehicle around and ran it through from the other end of the pipe. These results

are not in this report. The differential coils do not appear to have any significant advantage over our standard sensor coils.
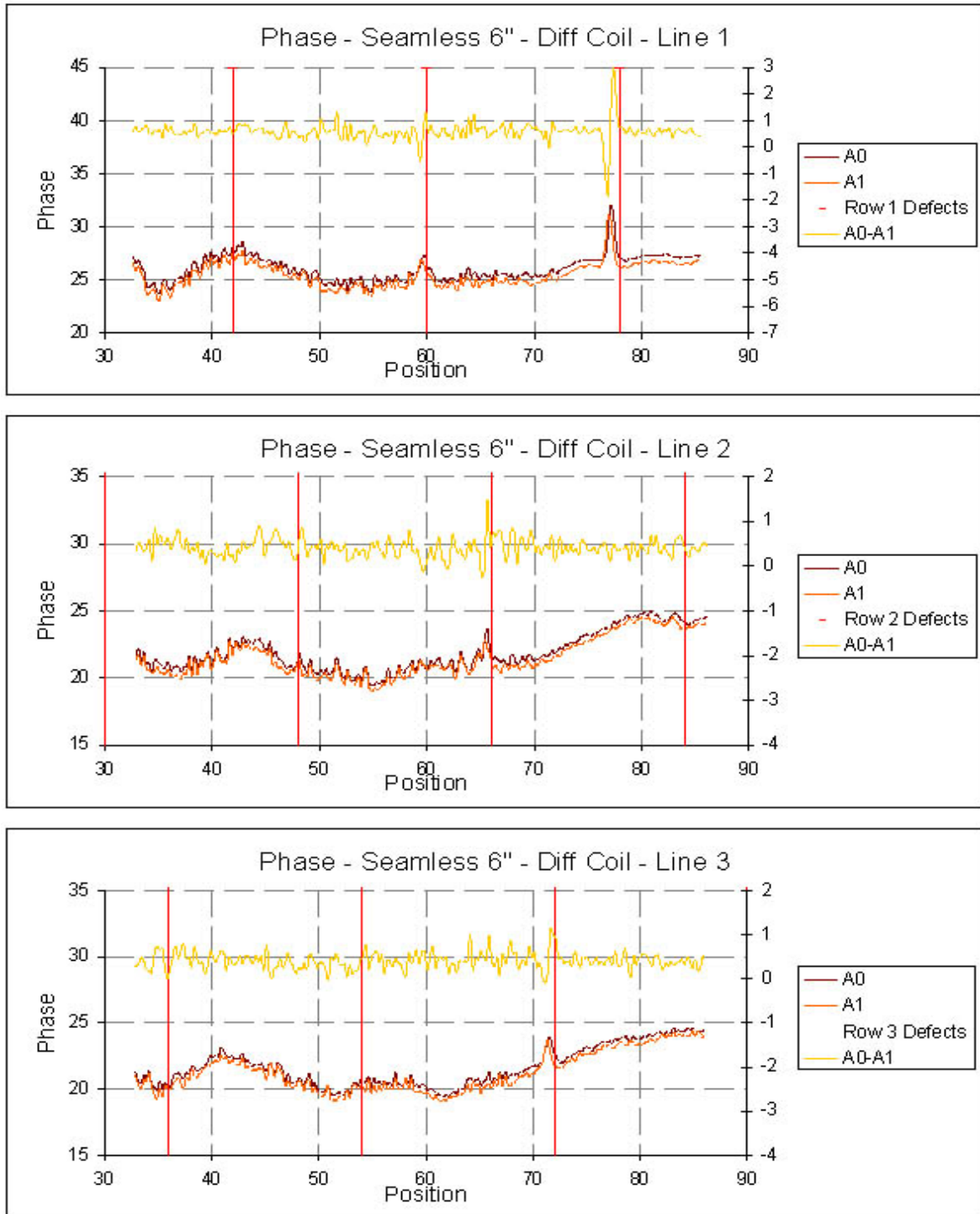
Figure 9: Results of scanning the 6" seamless pipe with differential coils.

Before beginning testing with exciter coil 5, we attached a 4' section of 6" PVC pipe to the starting end of the seamless pipe. It allowed us to take measurements from the zero mark and we were able to inspect the defects located at 24" and 30" without pulling the RFEC vehicle through from the other end.

In addition to coil testing, we standardized our exciter coil - sensor coil center-to-center distance to 15" based on the dimensions of the Explorer II platform. Prior to this standardization, the center-to-center distance for each test was based on pullout results of the individual exciter coils.

EXCITER COIL 5 TESTING
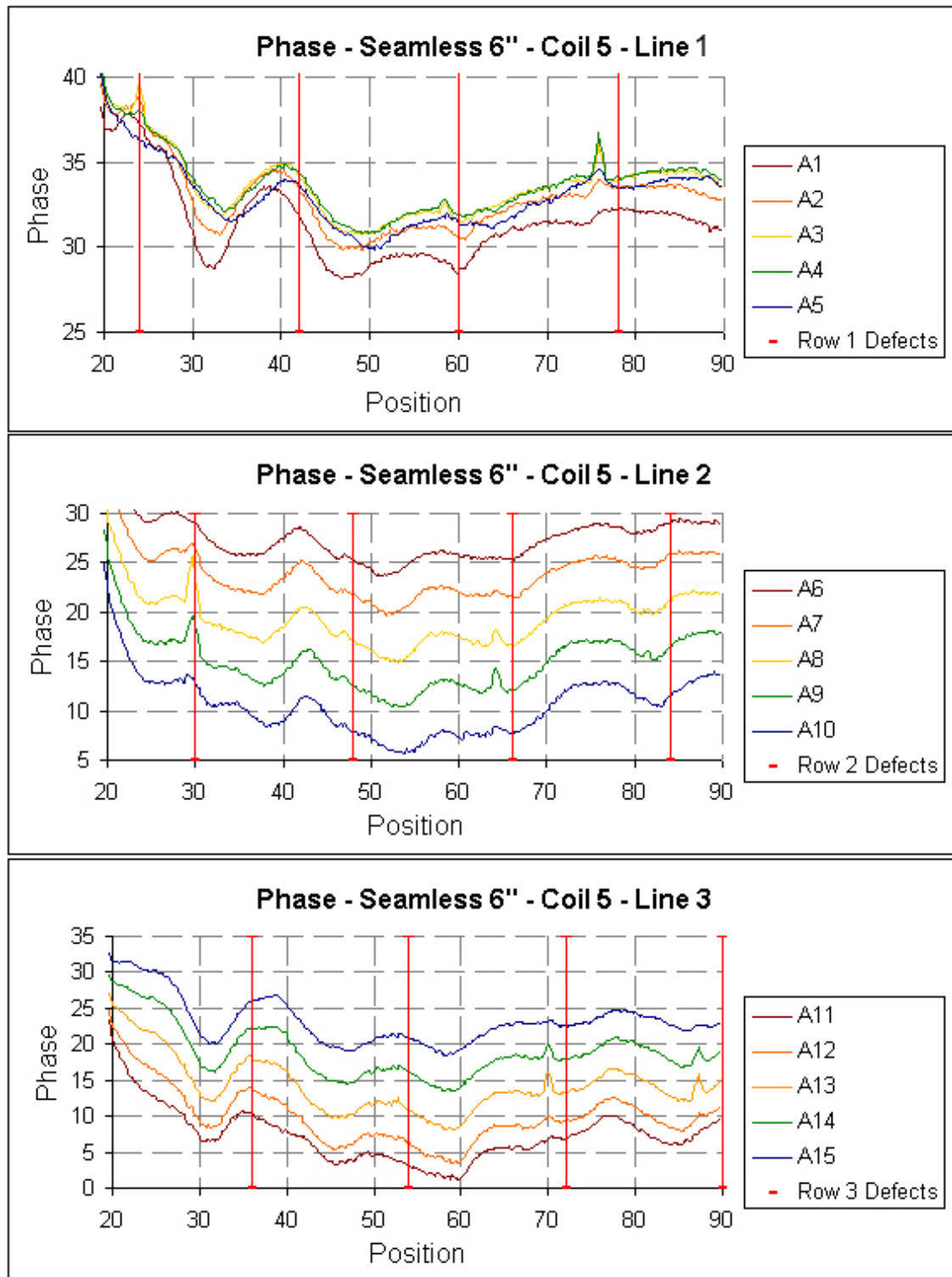
Figure 10: Results of 6" seamless pipe scan using Coil 5 with a mock module.

Figure 10 shows the results of scanning the 6" pipe with Coil 5 as the exciter coil. This test was performed with an imitation aluminum Explorer module between the exciter coil and pick-up coils. This test was conducted to ensure that the metal module would not cause an intolerable disruption of the RFEC signals. We were pleased with the results in Figure 10. The defect locations are marked with red vertical lines. An increase in the phase can be seen in at least one coil at most defect locations. The defects that were not detected are the 5%, ½" at 42" in line 1, the 30%, ¼" at 36" in line 3, and the 20%, ½" at 54" in line 3. None of these defects would be repaired in the field.

EXCITER COIL 6 TESTING
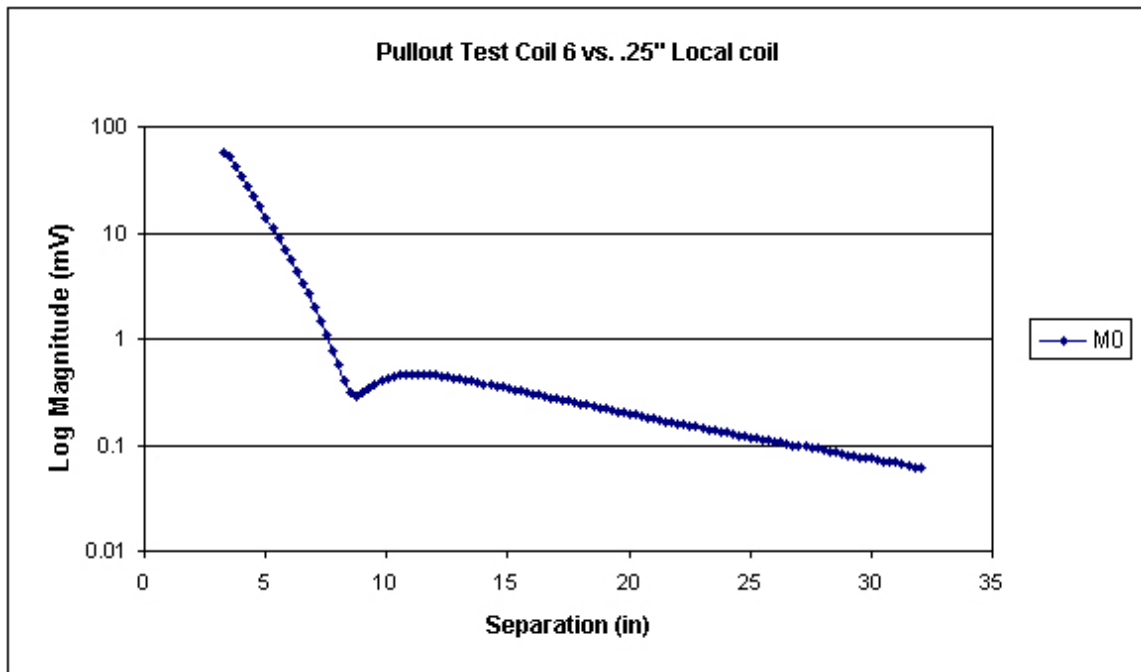
Figure 11: Results of a pullout test using Coil 6.

Upon completion of winding Coil 6, we performed a pullout test. The pullout test consists of starting the exciter coil and sensor coils close together and taking readings as they are pulled away from each other. The test shows where the direct field attenuates and the remote field signals will be the only detected signals. The log plot of the magnitude in Figure 11 shows the pick-up coils should be positioned at least 11" away from exciter coil 6. The strength of

the signal remains strong through about 20". Following the pullout test, we scanned the 6" seamless pipe using Coil 6. The results are shown in Figure 12.
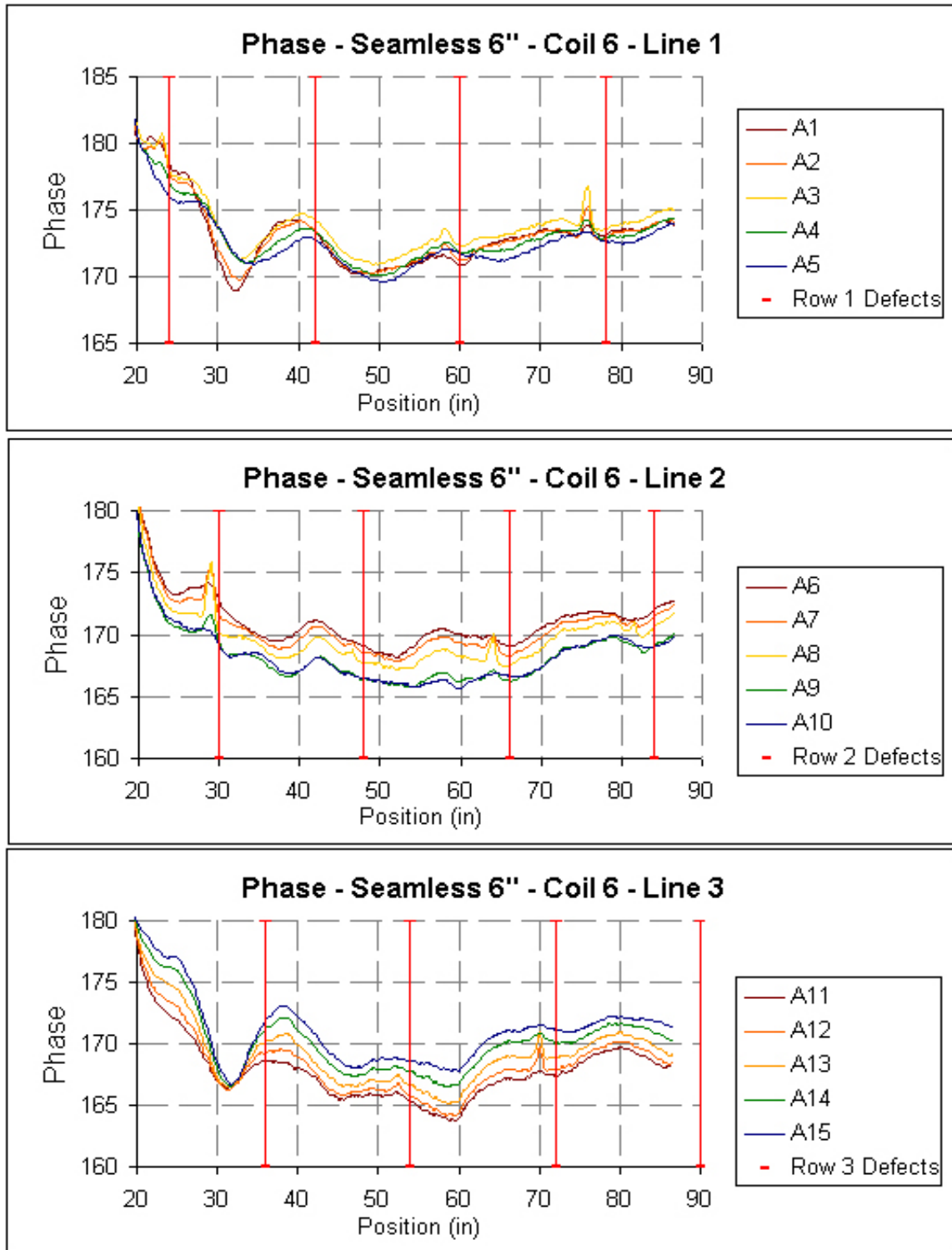
Figure 12: Results of scanning the 6" seamless pipe with Coil 6.

The figure above shows scanning results of exciter coil 6 in the 6"
seamless pipe. The results are similar to Coil 5 results shown in Figure 10. Coil 6
detected all the defects Coil 5 and in addition, detected the 20%, ½" defect at 54"
in line 3. In other scans with Coil 6, we have seen detection of all defects with the
exception of the 5%, ½" defect.

EXCITER COIL 7 TESTING

Coil 6 is made from 900 turns of wire across 4" of a 3.5" diameter roll. We
modified the geometry by winding the same number of turns across 2.5" of a 3.5"
diameter roll. This is Coil 7. Theoretically, the shorter exciter coil, 7, should have
a quicker attenuation of the direct field because the propagating fields are less
spread out across the length of the coil. We performed a pullout test on Coil 7 as
we did with Coil 6.
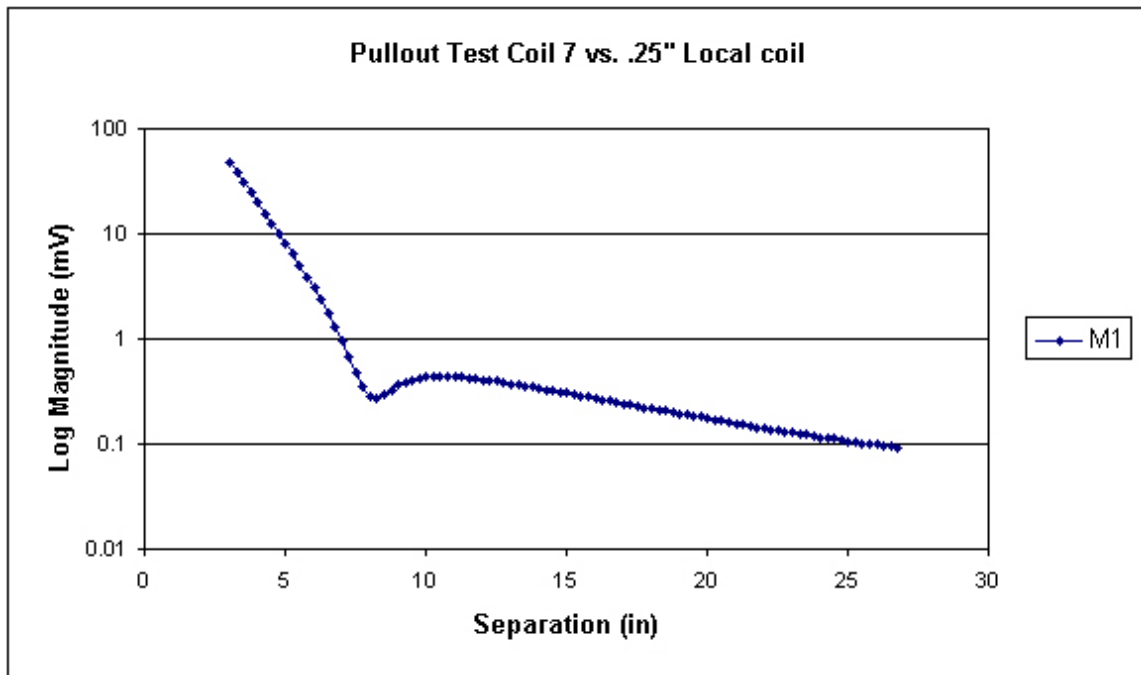
Figure 13: Results of a pullout test using Coil 7.

As we expected, the sensor coils can be positioned closer to the exciter
Coil 7 than Coil 6. The sensor coils should be placed at least 10" from Coil 7 for
inspection. This is 1" closer than Coil 6 placement relative to the sensor coils.
Results of the pullout test for Coil 7 are shown in Figure 13.
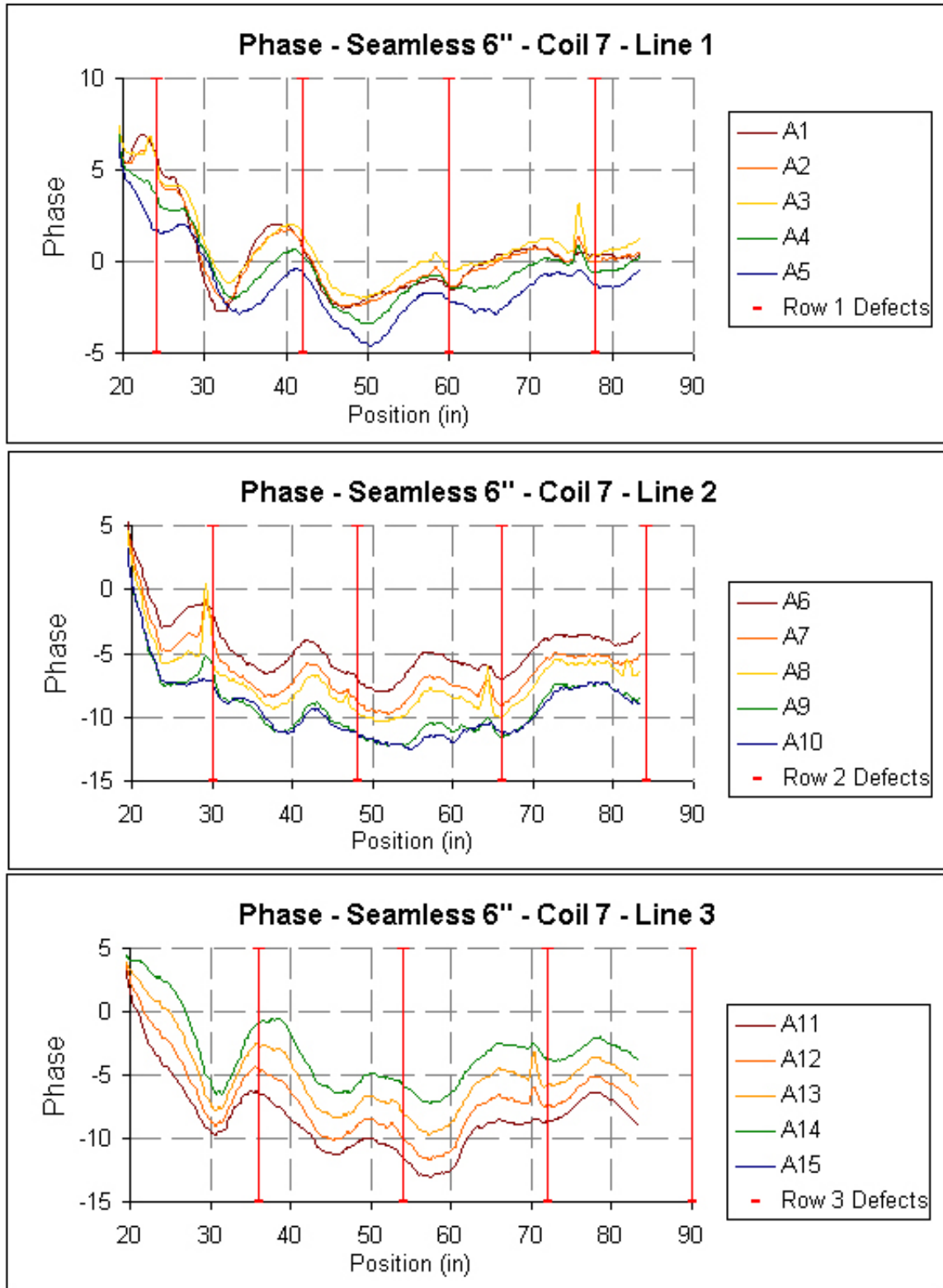
Figure 14: Results of scanning the 6" seamless pipe with Coil 7.

Figure 14 shows results obtained from scanning the 6" seamless pipe with Coil 7 as the exciter coil. To date, Coil 7 has been the only exciter coil to detect all 13 defects, including the 5% wt. Throughout the testing process, the data obtained from scanning the seamless pipe tends to follow the same trends. At the same time, there are also trends in the magnitude and phase data from the welded pipe scans. The patterns in the welded pipe differ from the patterns seen in the seamless pipe. We suspect the gradual rising and falling of the data is attributed to permeability variation in each of the pipes, but could not eliminate residual magnetic fields. In order to better understand the data and to have a set of data to use as the base, we set up a baseline test. We laid both pipes parallel to each other and ran subsequent tests using the same vehicle and lab equipment. The first baseline test results are displayed in Figure 14. We performed the first scan on the seamless pipe. Upon completion of that scan, we transferred the RFEC vehicle to the welded pipe and performed a new scan on the welded pipe. These results are shown in Figure 15 below.
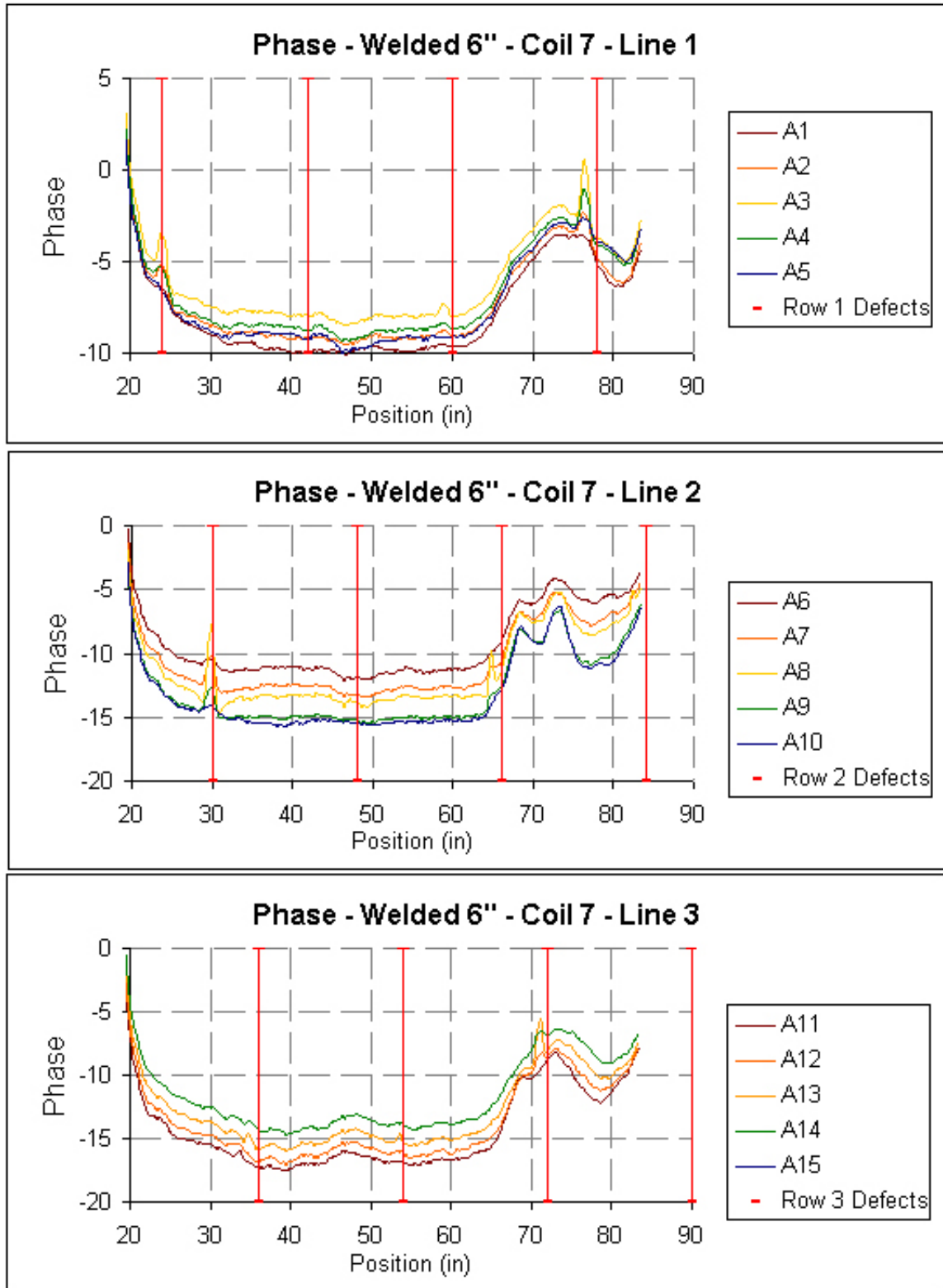
Figure 15: Results of scanning the 6" welded pipe with Coil 7.

ASSESSMENT OF EXCITER COILS

Table 1 below is a listing of all the defects, their location, depth, diameter, and shape as well as the detection ability of each of the coils. Check marks represent if the defect was detected. The X's represent the defect as not being detected by that particular coil. Coil 7 was the only exciter coil to detect all the defects. Coil 6 was able to detect all but the 5%, ½" defect. Coils 2, 4, and 5 were able to detect the 20%, ½" defect but did not detect the 30%, ¼" defect. The reason the 30% was not detected is that the diameter is only ¼" and we scan the pipe in ¼" steps. Most likely, the defect would be detected scanning in 1/8" steps. All in all, any of these exciter coils are sensitive enough for accurate detection of defects in an operating pipeline that would require repair.

Row	Location	Depth	Diam.	Shape	Coil 2	Coil 4	Coil 5	Coil 6	Coil 7
Row 1	24"	30%	1"	Round	✔	✔	✔	✔	✔
	42"	5%	½"	Round	✘	✘	✘	✘	✔
	60"	30%	½"	Round	✔	✔	✔	✔	✔
	78"	70%	½"	Round	✔	✔	✔	✔	✔
	96"	30%	1"	Square	✔	✔	✔	✔	✔
Row 2	30"	30%	¾"	Square	✔	✔	✔	✔	✔
	48"	10%	½"	Round	✔	✔	✔	✔	✔
	66"	40%	½"	Round	✔	✔	✔	✔	✔
	84"	30%	¼"	Square	✔	✔	✔	✔	✔
Row 3	36"	30%	¼"	Round	✘	✘	✘	✔	✔
	54"	20%	½"	Round	✔	✔	✔	✔	✔
	72"	50%	½"	Round	✔	✔	✔	✔	✔
	90"	30%	¾"	Round	✔	✔	✔	✔	✔

Table 1: Ability of drive coils to detect various sized defects [6 pt space]

Choosing the proper exciter coil for use on the Explorer II will be more involved than just selecting the coil with the best detection ability. It is important for the coil to make good use of available module space. Additionally, limiting weight and power consumption will be critical.

To date, we have tested a total of five exciter coils, 2, 4, 5, 6, and 7.The specs for these coils are listed in Table 2 below. Of the five, Coil 4 was the most undesirable because of its power consumption and size. Coil 2 is also undesirable based on size relative to the size of the robot module. We wound

coils 5-7 around a 3.5" spool to make better use of the module space. The inner diameter is large enough to fit electronic components inside of it yet small enough to wrap it with a protective shield for use in the pipeline. Coils 6 and 7 are rather heavy but were able to detect more defects than the other exciter coils. Coil 5 is a likely candidate because it strikes a good balance between weight and power consumption.

Coil Name	Inner Diameter (")	Length (")	# of Turns	Wire Gauge	Weight (lb)	Power Consumption (W)
Coil 2	2.375	3.25	2000	29	1.03	1.06
Coil 4	2.375	1	750	29	.35	6.62
Coil 5	3.5	4.25	1355	26	1.85	1.85
Coil 6	3.5	4	900	28	3.76	2.35
Coil 7	3.5	2.5	900	28	3.09	4.11

Table 2: Specifications of exciter coils tested.

We performed additional coil testing to determine the ability of RFEC to perform properly when operating on Explorer II. The first study consisted of running the lab equipment with an imitation robot module. The concern is that the modules of Explorer II, being metallic, could generate eddy currents within them, thereby deteriorating the remote field received by the pick-up coils. We did not see any significant loss in the magnitude of the remote field.

In order to design the drive coil module, we had to know what materials were appropriate to use as the backbone. The module would need to be strong in order to support the weight of the robot during vertical climbs but must not have a negative effect on the drive coil. Again, we had the concern of metal effects on the electromagnetic fields and performed a series of tests using various pieces of metal inserted into the drive coil. We concluded aluminum or stainless steel could be used without adverse effects on the sensitivity of the RFEC technique.

RUSSELL FERROSCOPE

Preliminary tests were conducted with the Russell detector boards in the welded 6 inch pipe. The Russell boards output information in in-phase and quadrate components. A computer program was written to convert the data into

amplitude and phase format for analysis. The program also allows the option to scale the data (necessary for use in the Russell data analysis program) and to average data over a fixed time length (useful for reducing noise levels and comparing data with the original lock-in amplifier).

The results of the first test shown in Figure 16 below are for two coils pulled at a rate of about 1.5 inches/second. The complete defect line was scanned in 100 seconds compared to the lock-in amplifier which took about 90 minutes. The length of the lock-in scan is due mostly to the multiplexer which sequences through the 16 pickup coils and the associated settling time between channels.

For the first 250 measurements and the last 300 measurements the coils were stationary and show that the electronic noise is acceptable, causing a jitter of about .3 degrees in the phase data. However the noise level increased dramatically after the system began moving. This was the first test conducted with the Russell boards where data was collected while the coils were moving. We believed that the noise was due to mechanical vibrations of the pickup coils interacting with the residual magnetic fields in the pipe itself. Tests with the system designed to be more rigid and pulled smoother verified this conclusion.
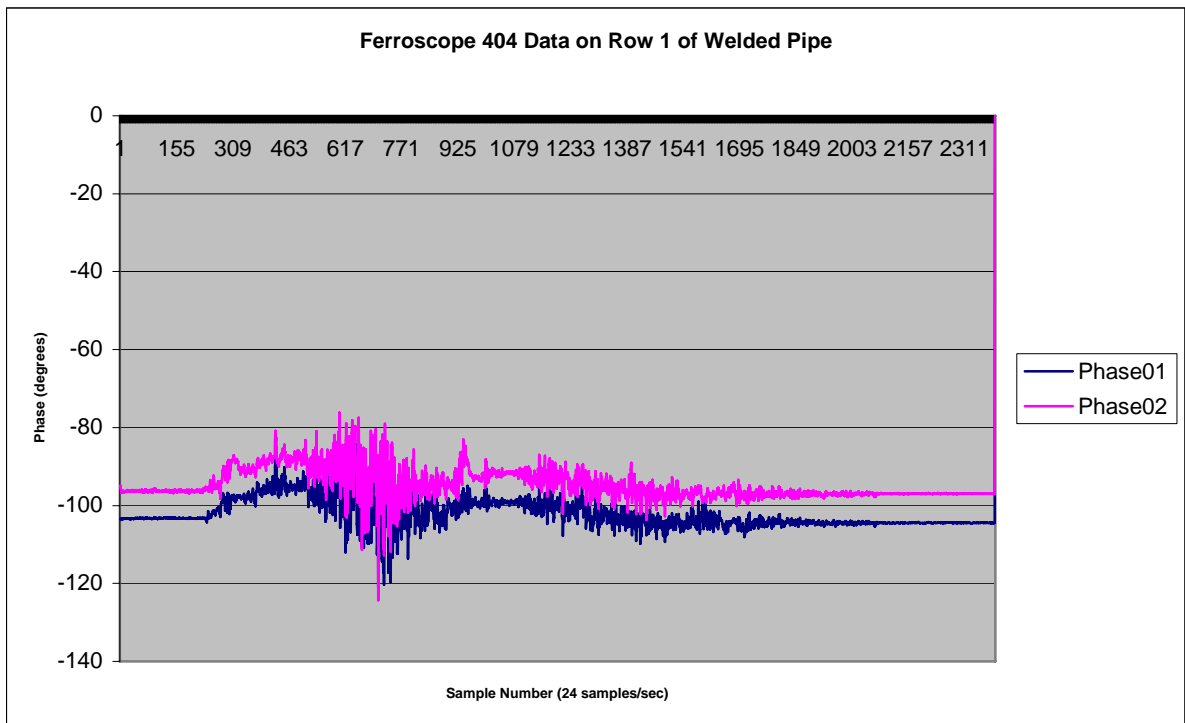
Figure 16: Data from defect line 1 using the Russell board.

We rebuilt the part that the two pick-up coils were mounted to by adding wheel supports. The wheel supports enabled a smooth pull through the pipe by reducing the mechanical vibrations of the coils and avoiding any scraping against the pipe wall. Data taken with the rebuilt system is shown in Figure 17. We were able to detect two defects. The sizes of these defects are 1", 30%wt and ½", 70%wt.

Ferroscope 404, Welded Pipe, Wheel Support
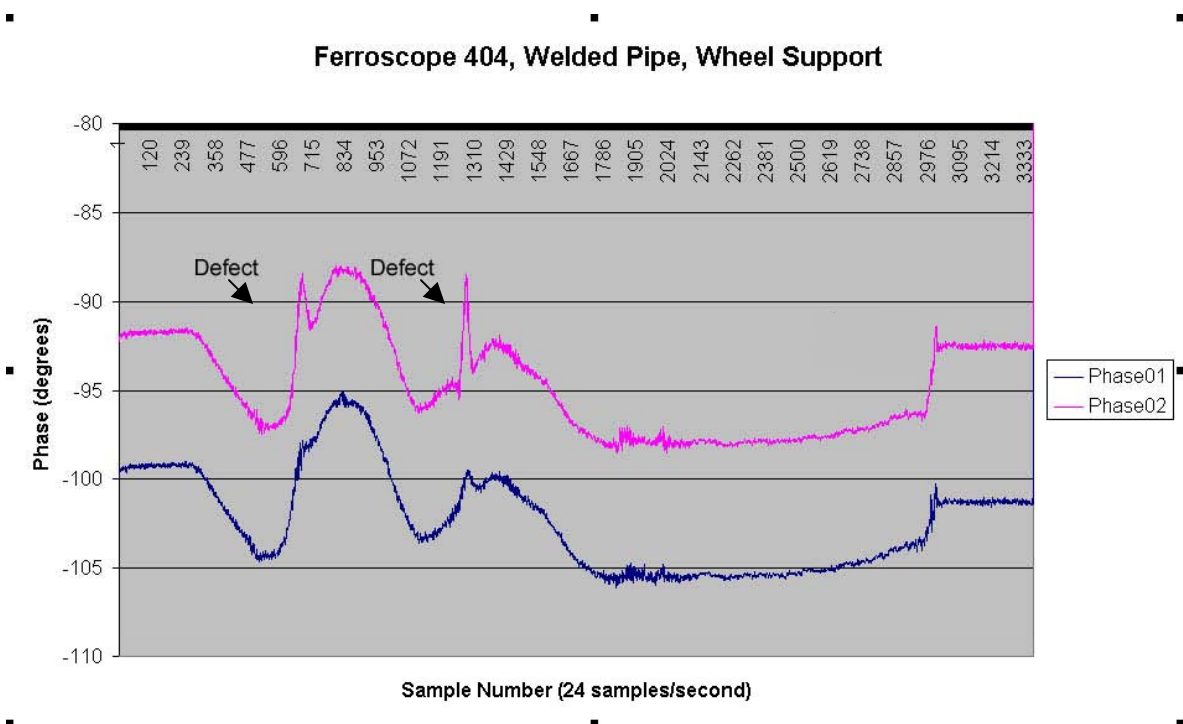
Figure 17: Phase data from defect line one of the seam welded pipe using the Russell boards with wheel supports.

Welded Pipe, Lock-in Amplifier
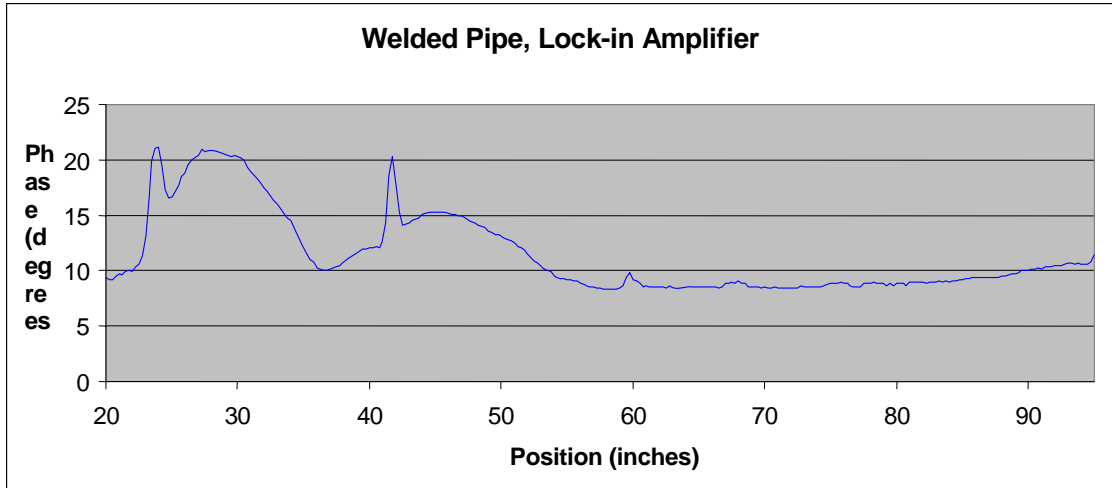
Figure 18: Phase data from defect line one of the seamless pipe using the Lock-in Amplifier.

After inspecting defect line number one using the Russell boards, we noticed that the noise in the data appeared greater than for the lock-in amplifier that we had been using. For comparison purposes, we repeated the inspection using a lock-in amplifier, shown in Figure 18. An rms calculation of noise levels in the phase data gives .21° rms for the Russell Boards and .16° for the Lock-in Amplifier. This normally would indicate that the two are very similar; however, noise from the Russell board comes in bursts. From the lock-in, noise is continuous. The peak burst for the Russell board is 1° peak-to-peak and for the lock-in is .2-.3° peak-to-peak. These differences are the reason that the ½", 30% defect is detected by the lock-in amplifier as shown in Figure 18 but not detected by the Russell board in Figure 17. In actual application this should not be a serious concern since the flaws of interest would be larger that this.

We also conducted tests using the Russell boards while driving the exciter coil with a square wave. The motivation for using a square wave rather than a sine wave is that the square wave drive circuitry requires less power. The tests were performed at various frequencies between 5-95Hz. The results at 25, 65, and 85Hz are shown in the figures below.
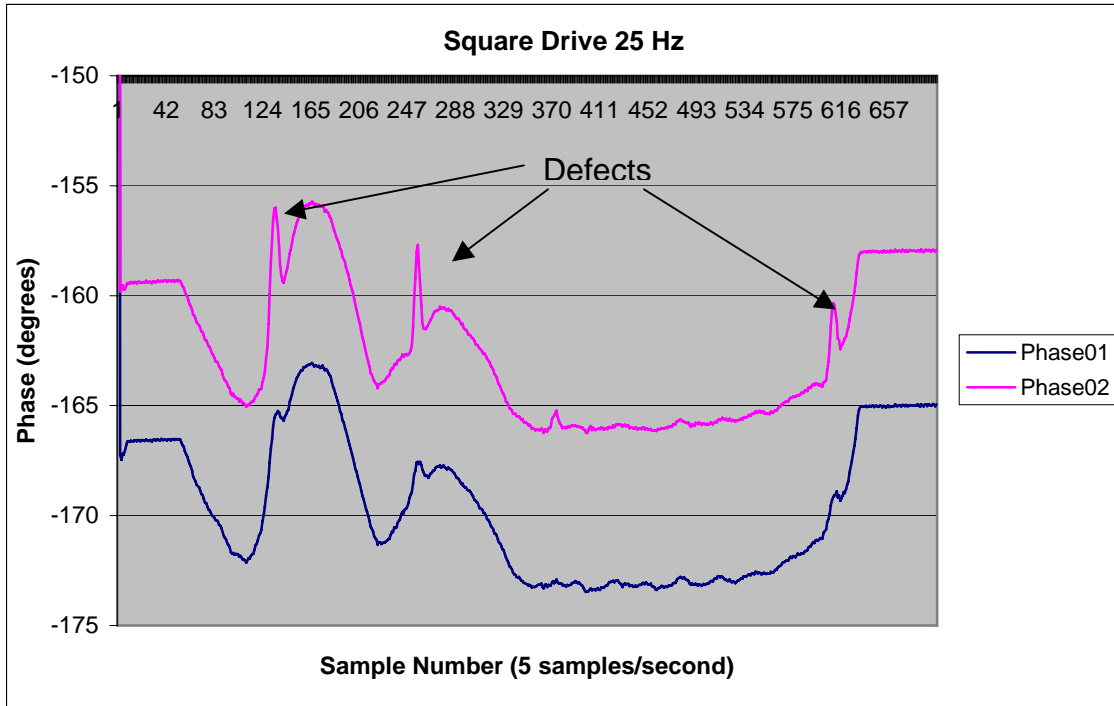
Figure 19: Phase data taken while driving the exciter coil with a 25Hz square wave.
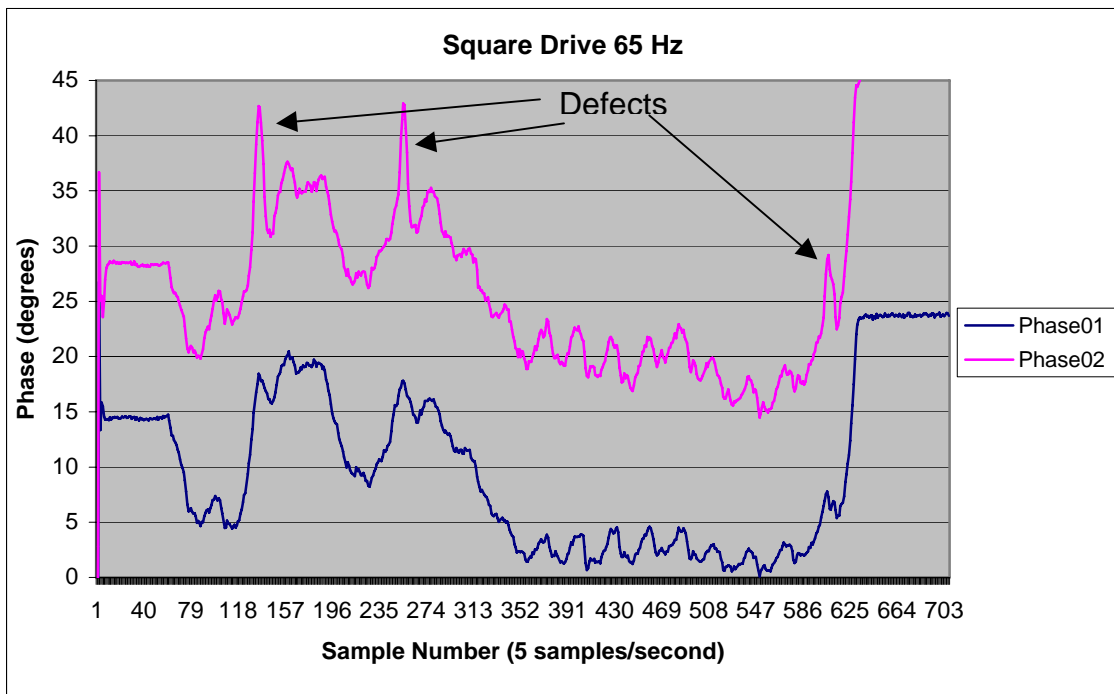
Figure 20: Phase data taken while driving the exciter coil with a 65Hz square wave.
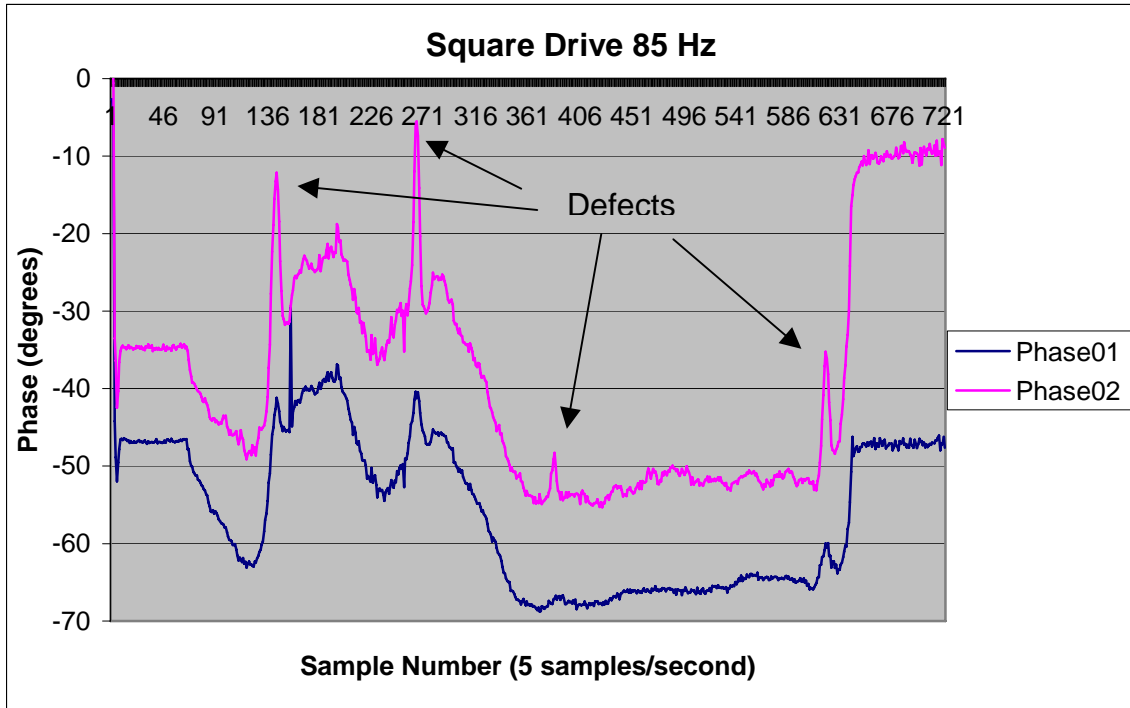
Figure 21: Phase data taken while driving the exciter coil with an 85Hz square wave.

Results of the 25Hz scan, shown in Figure 19, show 4 of 5 defects. Noise levels look reasonable. Starting at 45Hz and up to 75Hz, there was quite a disturbance in the noise. It seems to be periodic and we suspect it may be interference from 60Hz signals created by standard electronic devices (lights, computers, etc.) We only detected 3 of 5 defects during the 65Hz scan, shown in Figure 20, but it is interesting to note that the amplitude of the defect signals is considerably larger, about 3x. The amplitudes of the defect signals in the 85Hz in Figure 21 are 4-5x larger than the signals in the 25Hz test. The periodic type noise is reduced in the 85Hz test and 4 of 5 defects were detected.

We have observed that changes in permeability, the magnetic property of the pipe, affect the amplitude and phase response of the RFEC. To date we rely on the small lengths of the artificial flaws to distinguish between flaws and permeability changes. In Figure 22 below the sharp spikes from coil 2 (Phase02) at 121, 250, 370, and 601 are artificial flaws while the gradual peaks at 161 and 281 are permeability changes caused by residual stresses and possibly local residual pipe magnetization. We realize that real corrosion can be much longer

and that it may be more difficult to distinguish between them.
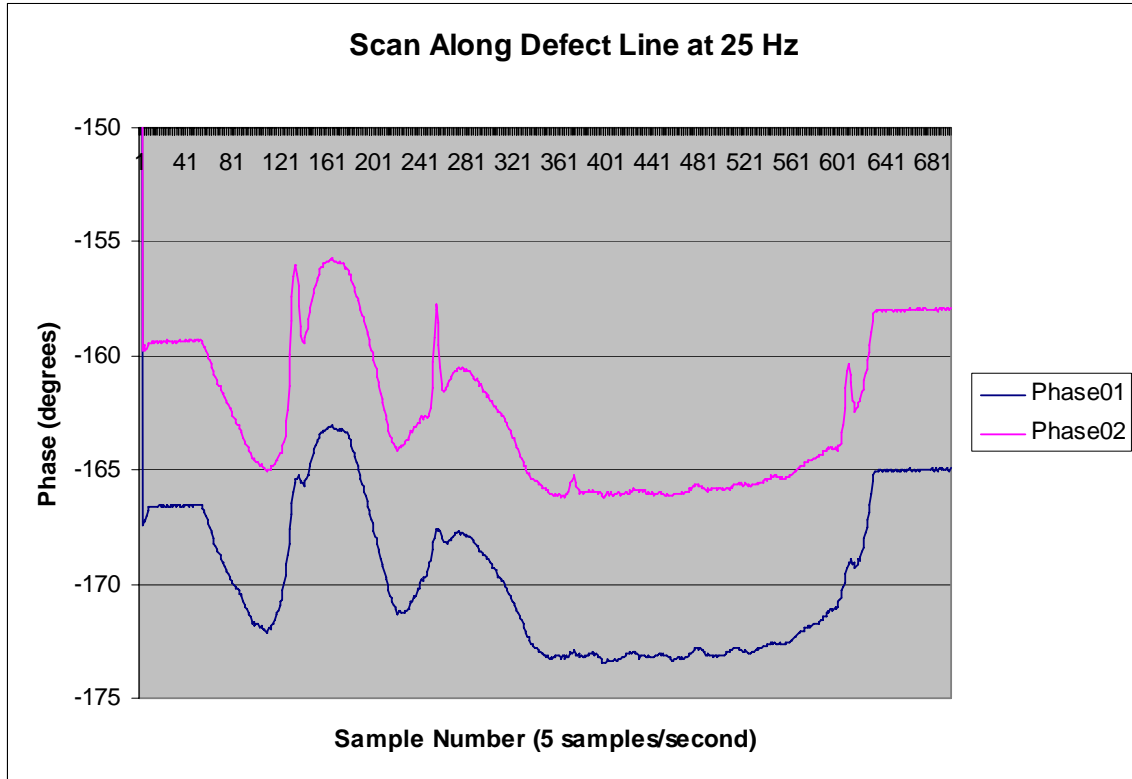
Figure 22: Defect scan at 25Hz

It is possible that analysis at several frequencies may help. The first step was to look at phase information as a function of frequency. The magnitude of the phase deviations at three artificial flaw locations was measured at different frequencies and was found to increase linearly with frequency up to 75 Hz. The results are shown in Figure 23. Flaw one is 1" diameter flat bottom 30% deep, flaw two is ½" diameter round bottom 70% deep and flaw five is 1" diameter round bottom 30% deep. There is a sharp increase at 95 Hz and then there is no detectable flaw signal at higher frequencies. The flaws do show up in the amplitude signal indicating that the analysis should be conducted in the complex plane.
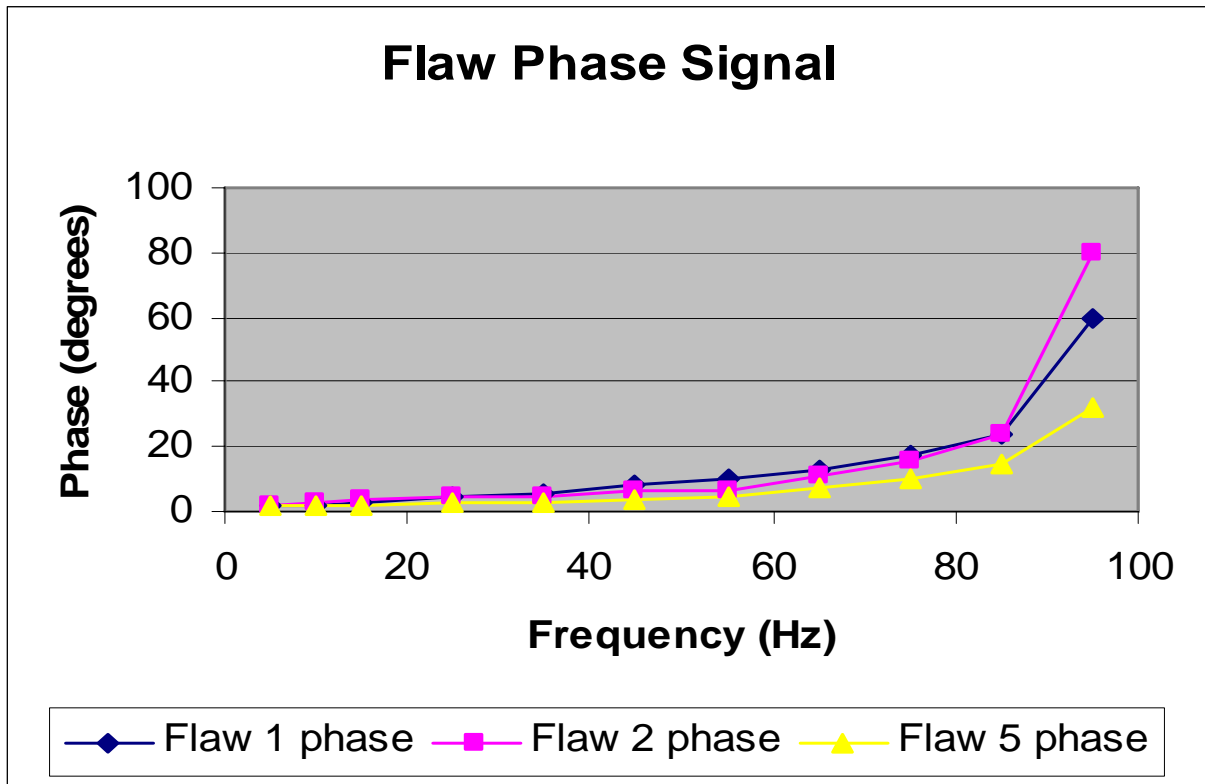
Figure 23: Flaw phase signal

The difference in phase between two locations with different permeability was plotted against frequency and found to also be linear with a sharp increase at 95 Hz. This plot is shown in Figure 24. The similarity of the responses indicates that it may be difficult to distinguish between permeability and gradual thickness changes using phase alone. We expect better results analyzing data in the complex plane.
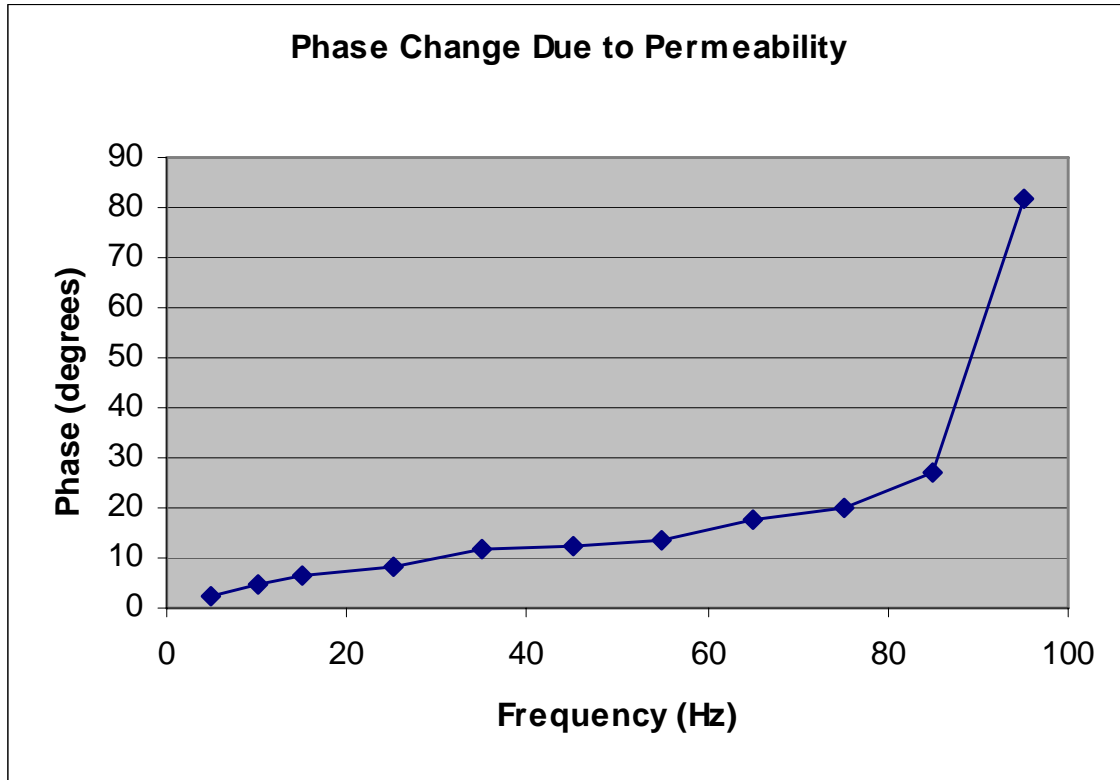
Figure 24: Phase change due to permeability

BENCHMARK II

During the week of January 9th 2006, GTI traveled to Battelle Memorial Laboratories in Columbus, OH to participate in the second benchmarking demonstration. We would have liked to have taken a partial or complete build of our module design but time did not permit us that ability. The final design review was not completed until the 16th of December 2005. We did not have enough Russell electronics to run more than two pick-up coils and therefore had to perform the blind tests using our laboratory hardware. We did run the Russell equipment for demonstration purposes. It took approximately 7 minutes to scan 23' of Pipe 3. This is an average speed of .66 in/sec which was determined by the speed of the tow motor, not the speed of the technology. The results of the scan are shown in Figure 25.
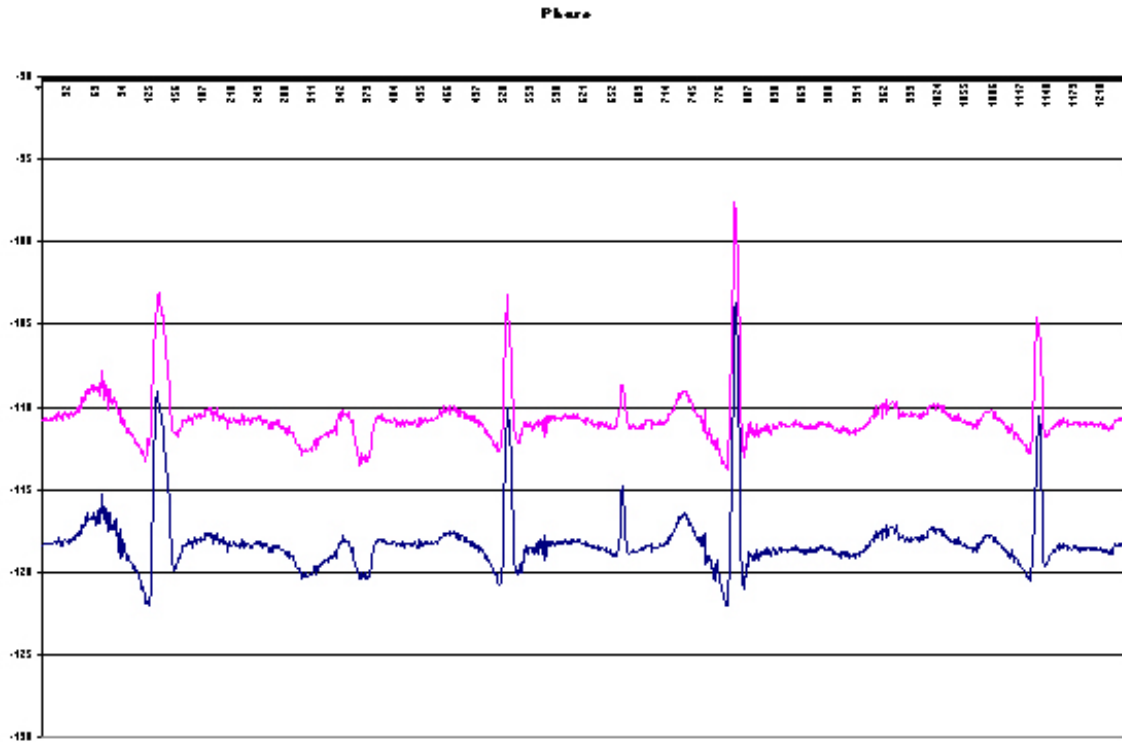
Figure 25: Results from scanning Pipe 3 using Russell equipment.

The data in Figure 25 is unfiltered – filtering will reduce the noise - and somewhat noisier than results obtained with a lock-in amplifier but is sufficient for its purpose.

Using laboratory equipment, we blindly inspected three 8" pipes, one of which contained a section of natural corrosion. The data from each pipe was later analyzed each by a different member of the GTI team and was not altogether consistent in the final reporting. Pipe 2 showed excessive scatter and Pipe 3 had a calibration error. The natural corrosion section was in Pipe 1 and was reported to within 5% of its actual depth. The answer key of one of the natural corrosion patches is shown in Figure 26. GTI's interpretation of data from the same scanned area is shown in Figure 27. There is excellent correlation between the two figures. Table 3 shows various defects from the benchmark. The pictures in the left column are color plots as shown on the answer key. The pictures in the right column are color plots from GTI's analysis program.
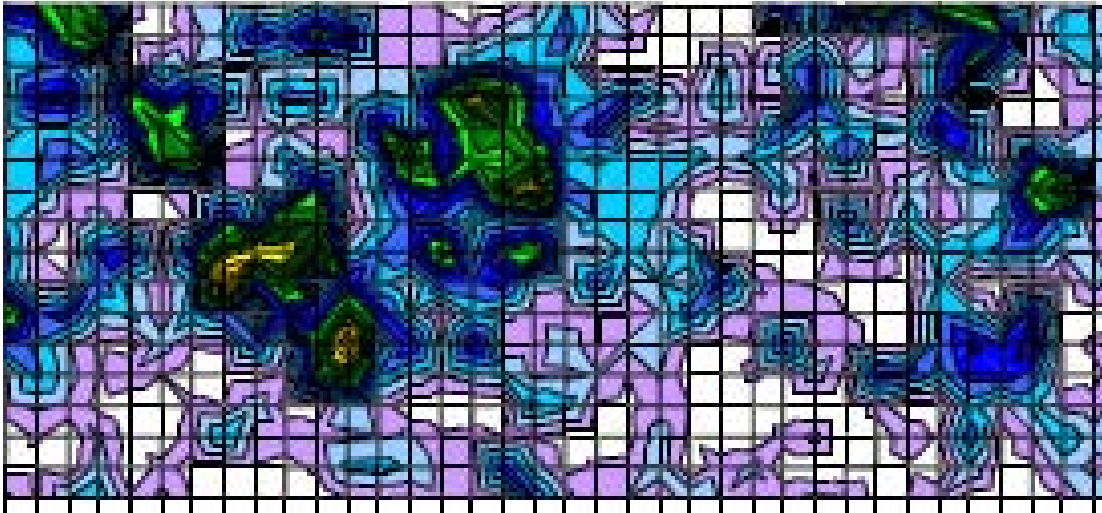
Figure 26: Actual Corrosion
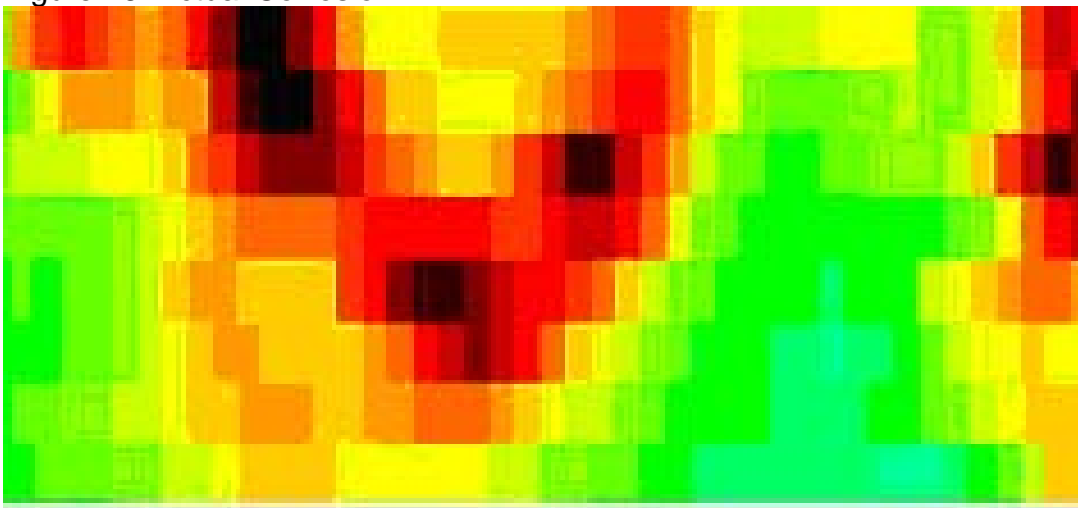
Figure 27: Corrosion as detected by GTI

Benchmark Corrosion Map	GTI Corrosion Map
Defect P1-12	
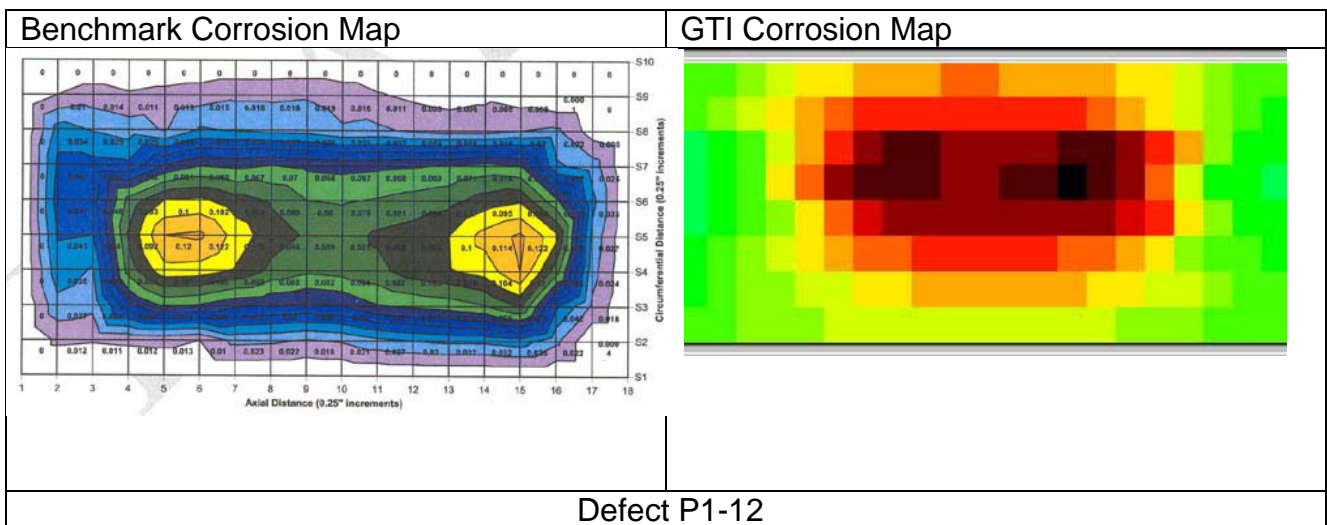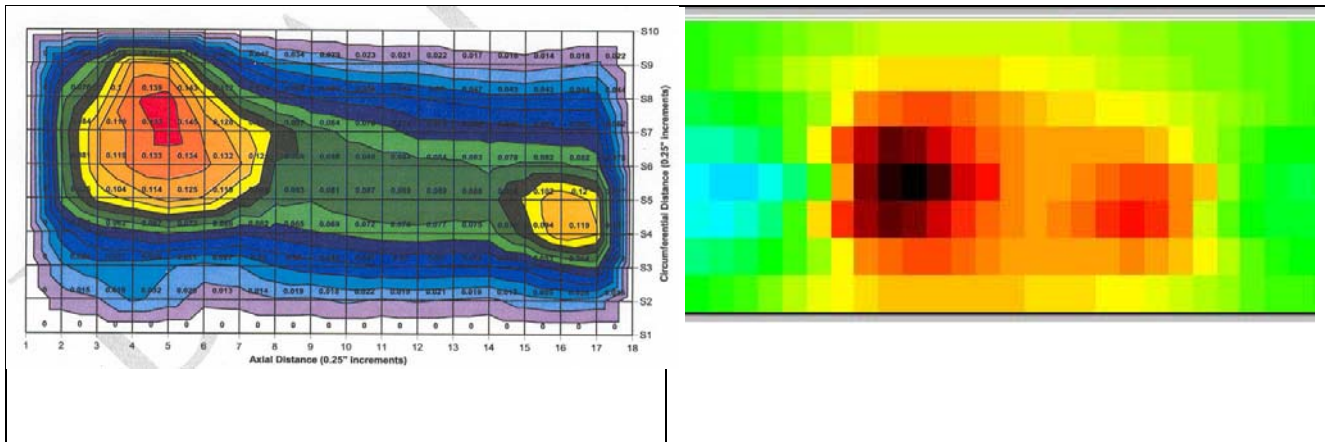
Defect P1-18
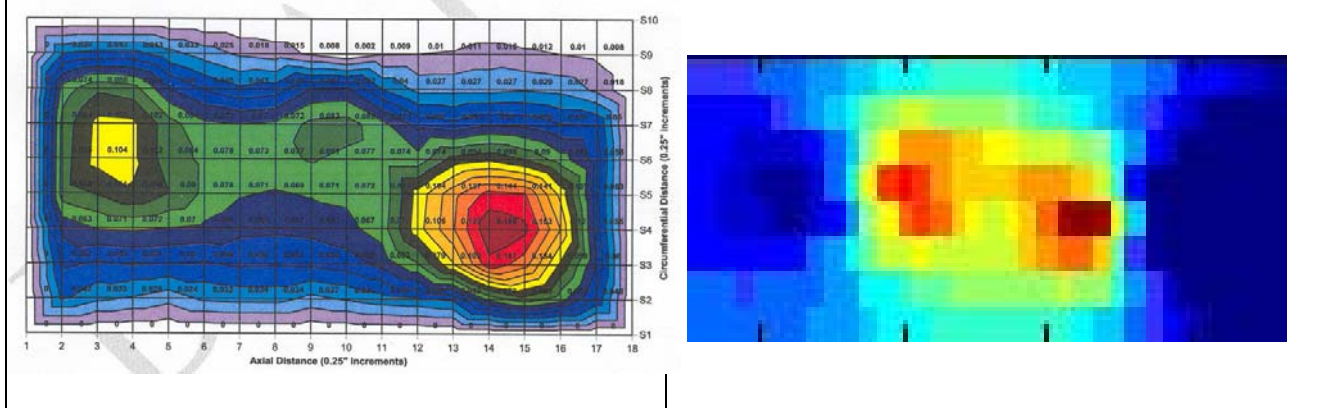
Defect P2-09
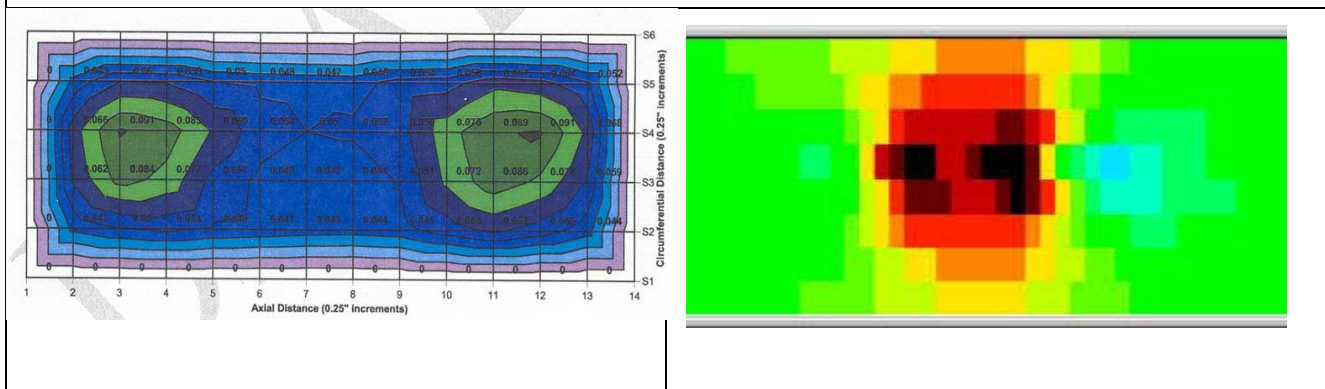
Defect P3-18
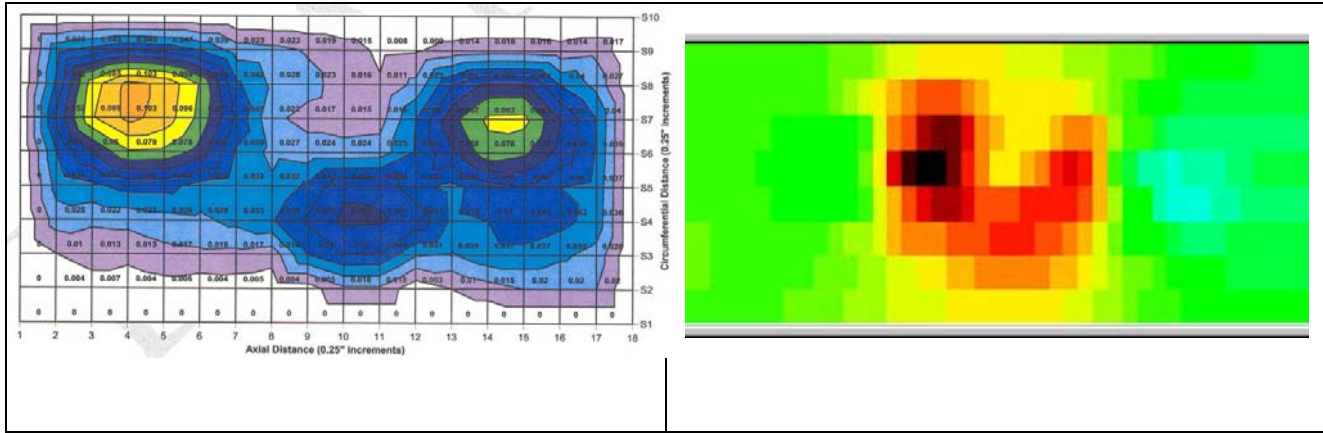
Defect P3-21

Table 3: Actual defect color plot vs. GTI color plot.

MECHANICAL DESIGN

The design process for the pick-up coil module started early in the life of the project. Multiple revisions were necessary. Three original designs were created using a 3D modeling program and were presented at the mid phase design review. One of these was chosen to go forward for the final design review. Upon the news that DOE-NETL funding would stop at the end of Phase II due to termination of the DOE infrastructure reliability program, GTI rescoped the work and changed the target range from 6-8" to 10-16" pipe diameters. GTI again revised the mechanical design.

There were certain parameters guided by the robot design and the technology itself. Sensor coil orientation was of great importance requiring the design to maintain the sensors parallel to pipe wall at any given diameter. For uniformity of measurements, it was also preferred that equal distances be maintained between the sensors. The design should also be compliant to dents, welds, and pipe ovality, and allow the sensor to move <u>forwards or backwards</u>. In order to develop a device capable of satisfying the requirements, it was found that each sensor arm should have a single rotation point. Each progression of the design used the radius of the module as the lever arm as opposed to lever arm designs that would take up the length of the module and occupy space that could otherwise be used to house electronics.

One of the first designs featured arms that curled around a central cylinder. The sensor coils were attached to the end of these curved arms which were allowed to rotate from a base plate. Figure 28 shows a partial model.
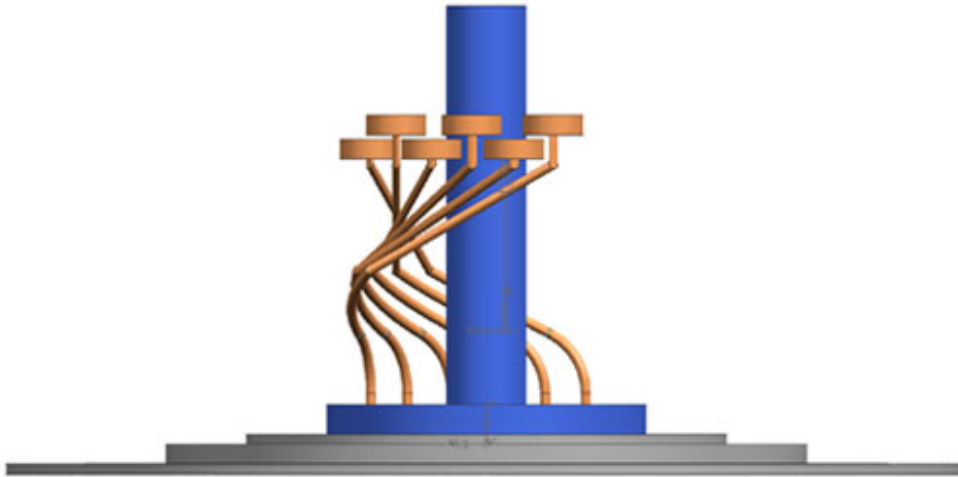
Figure 28: Early version of design.

The arm lengths were alternated so that the sensors nested into two circles allowing the module to house a greater number of sensors. Figure 29 shows this particular design from the top, in the 12" position.
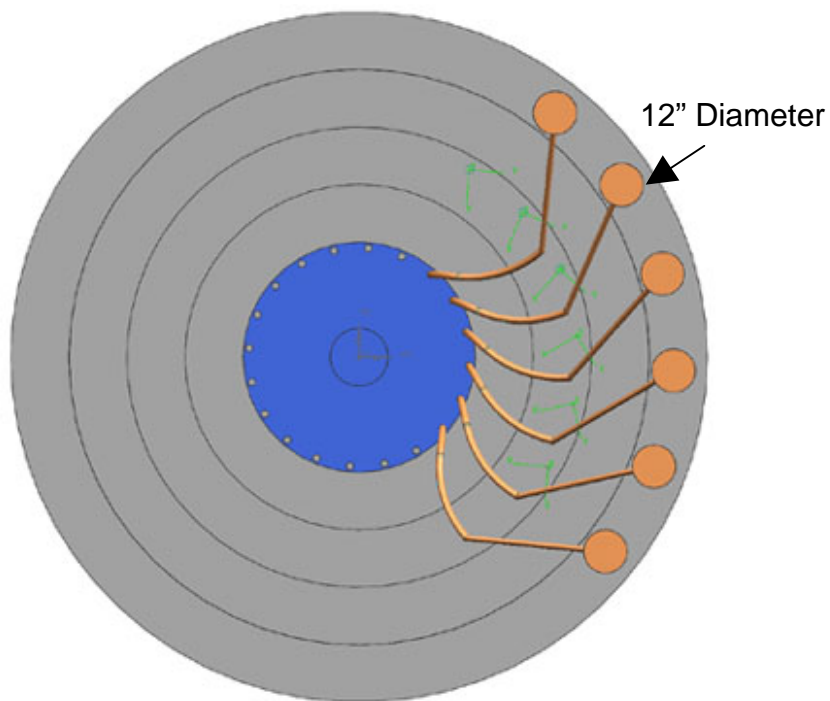
12" Diameter

Figure 29: Top view of the early design.

The blue circle represents the base plate, which measures 4" in diameter as required by the Explorer II specs. Each grey ring signifies and additional 2" added to the diameter with the outermost ring being 12" in diameter. As the base of the arms rotate in the plate, the ends of the arms are able to travel to nearly 12".

The design evolved slightly and the arm profile was altered. The next three figures display the changes. This version was presented at the mid phase review meeting.
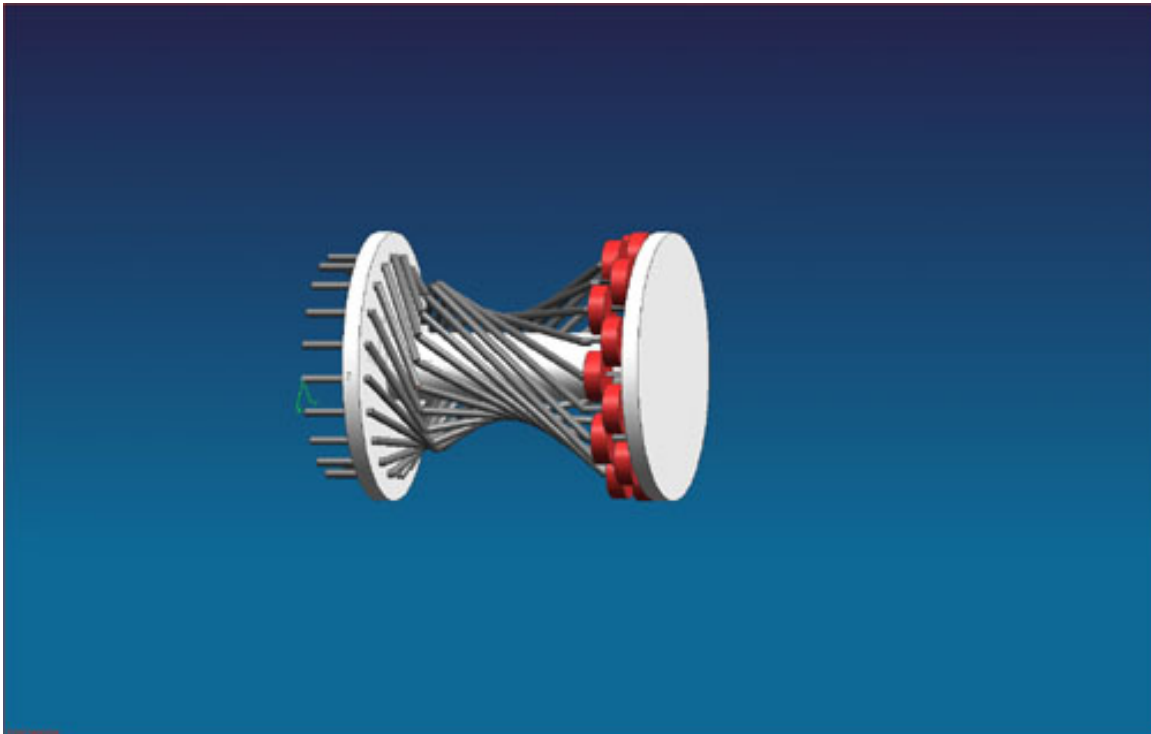
Figure 30: Design 1, side view, arms closed.

Figure 30 above shows the arms in the nested or closed position. The close limit is determined by interference between the spring steel arms and the tube running thought the center of the module. The tube served as a "backbone", wire conduit, and motor housing.

As the motor rotates inside the tube, it drives a sun gear (not shown) that rotates individual planetary gears at the base of each arm. Figure 31 shows the arms as they begin to open. As each arm is rotating, the sensors (red) are driven out in a uniform manner with equal spacing between each one and each at the

same distance from the center. The fully extended position is shown in Figure 32.
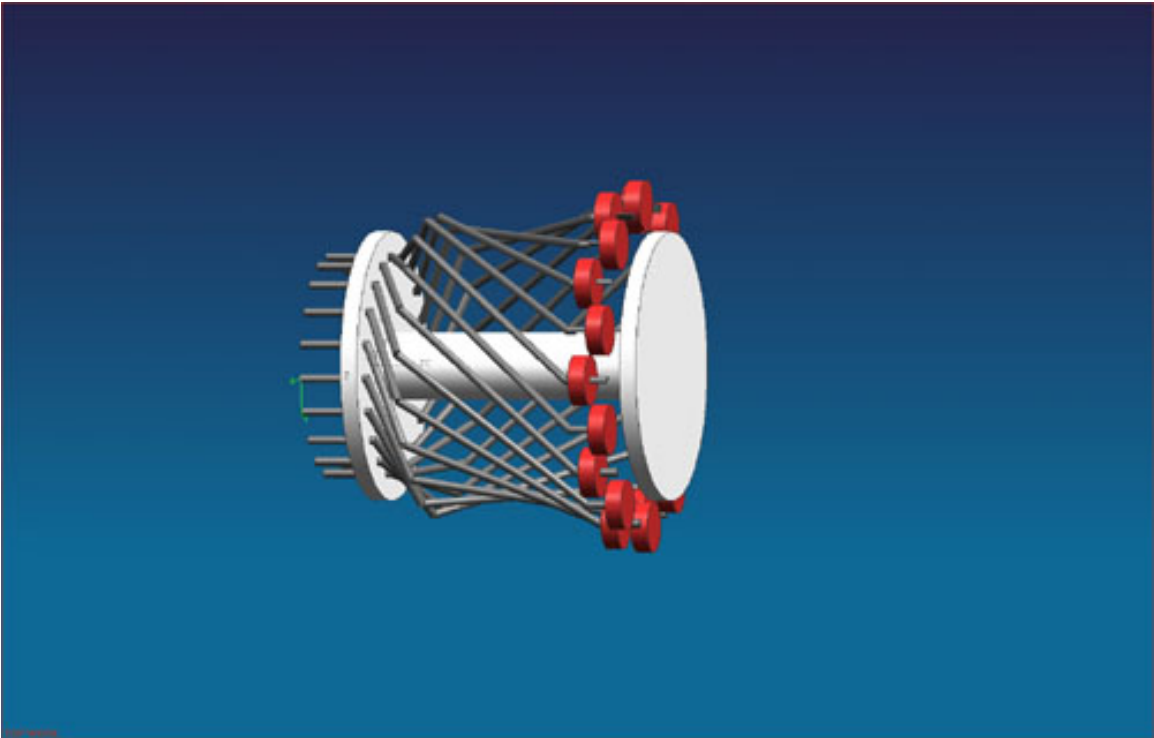
Figure 31: Design 1, side view, arms partially open.
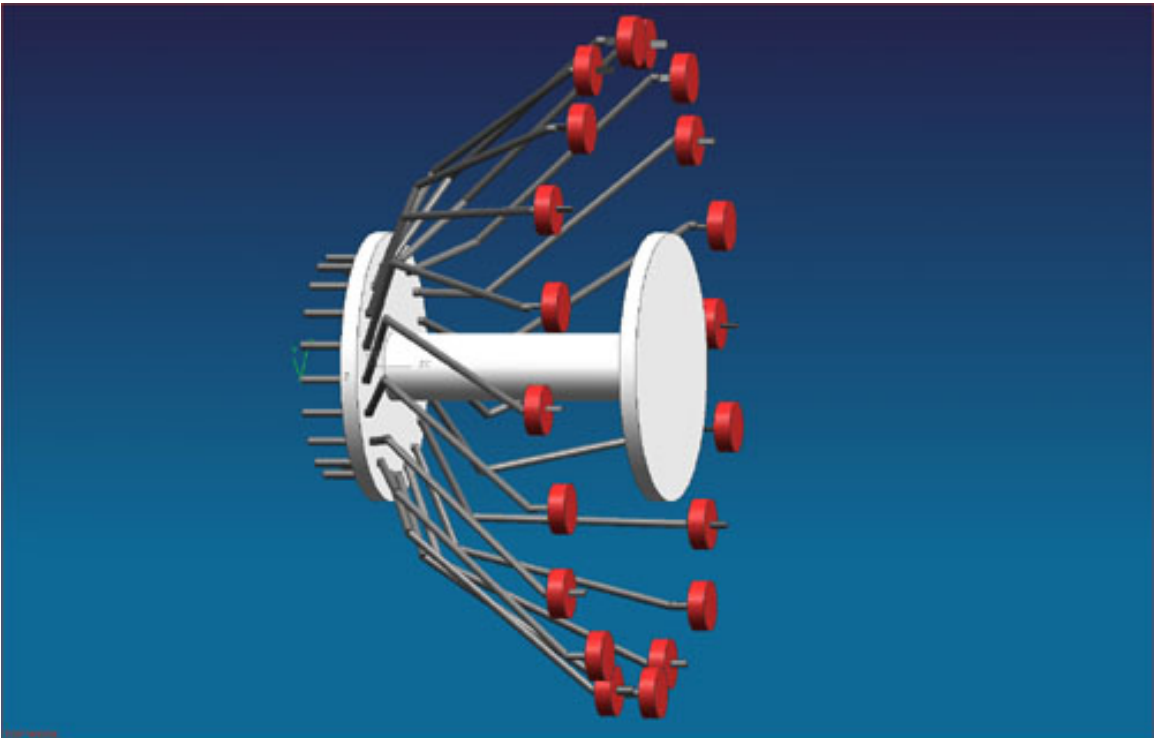
Figure 32: Design 1, side view, arms completely open.

The problems we encountered with the previously shown module were the lack of available space for electronics and complexity of manufacture. The swing of the arms required so much module space remain vacant that there was little room left for electronics. Each individual arm required precise construction which would have driven the building costs too high.

The next evolution of the module design featured electronics boards as the arms. This concept decreased the overall length by 30% and incorporated the electronics in the arms. A 2-D sketch of this design is shown in Figure 33 to portray the compactness of the design.
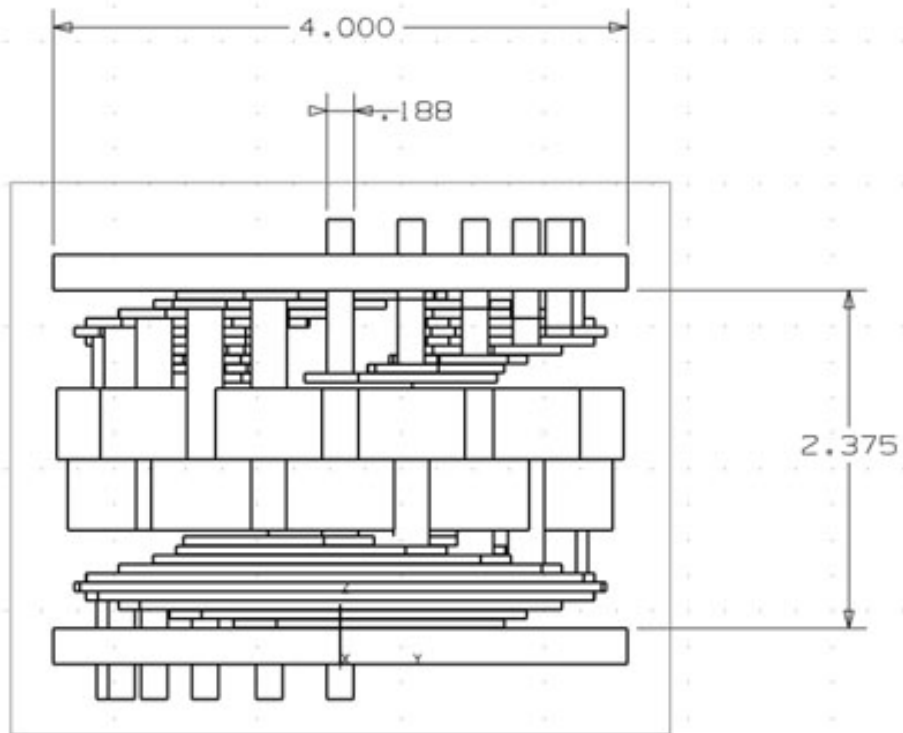
Figure 33: Design 2, 2-D sketch, side view.
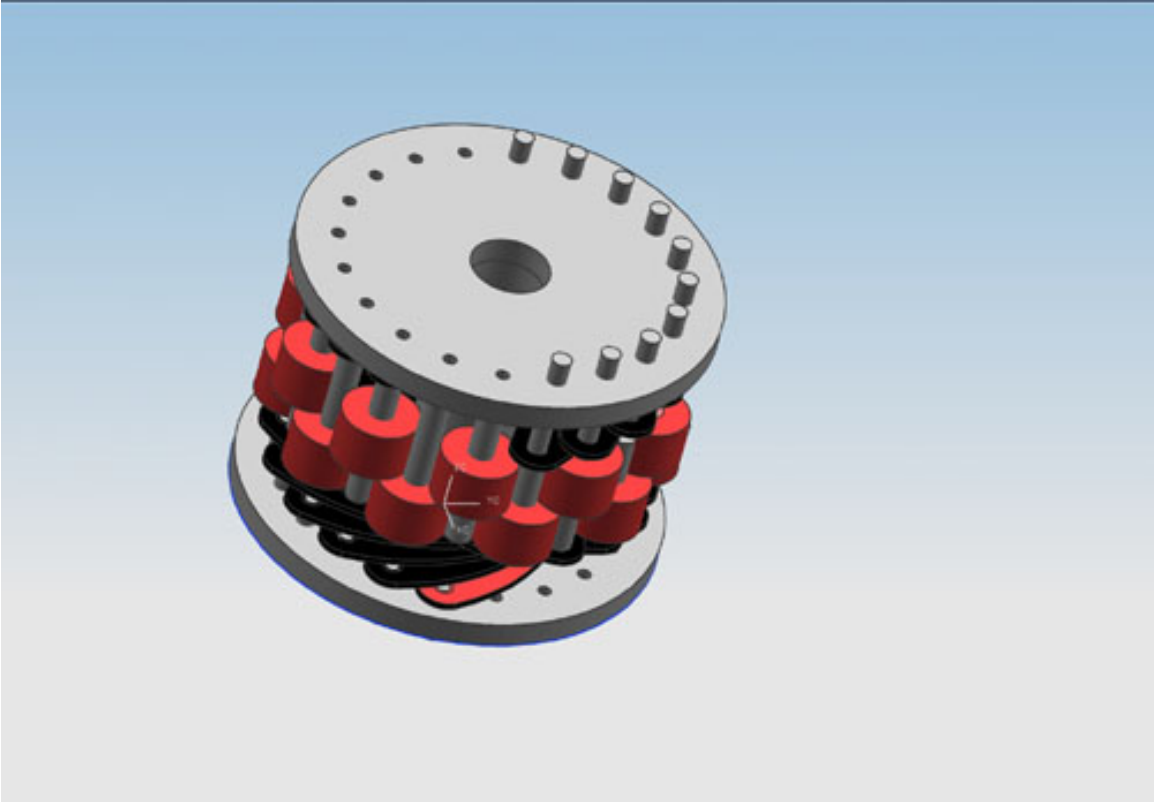
Figure 34: Design 2, isometric view, closed.

Figure 34 above, shows the 3-D drawing. The design introduced two arrays of 10 coils which are easier to see in Figure 32. Interferences prevented all 20 arms being mounted from one end plate so they were split and open opposite each other. Motion of all 20 arms was achieved using a single motor to maintain the rate of expansion and uniform separation.
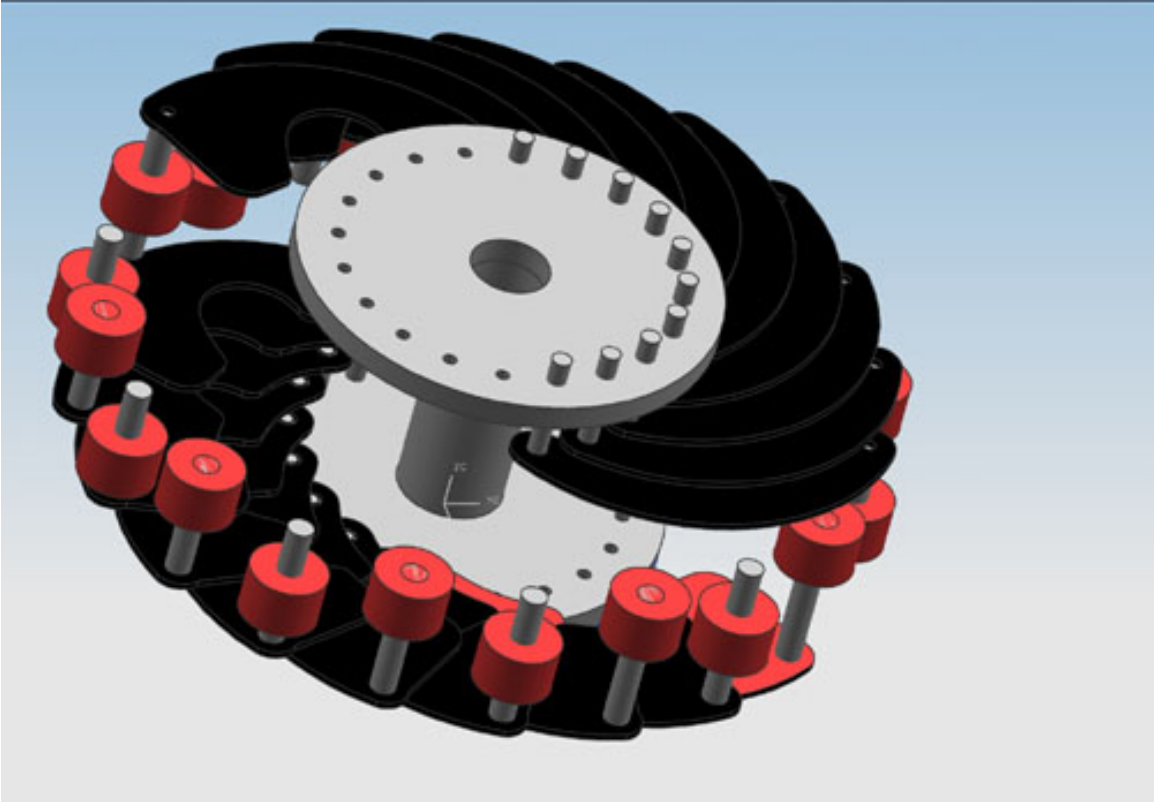
Figure 35: Design 2, isometric view, partially open.

The shape of the arms were a result of the design itself. Although the face area was made as large as possible, provisions had to be made for the center rod of the module. Additionally, the overlap seen by each arm at full extension prevents them from slipping past one another ensuring the arms will be able to be retracted. This feature is evident in the next two figures. Figure 36 give a good indication of the separation between each set of arms. This separation, although forced by the design, helps reduce the amount of gas flow blockage. Even if there were not an axial spacing between the arrays, the module would create no more blockage than an orifice meter. Figure 37 shows the uniform spacing of the sensors.
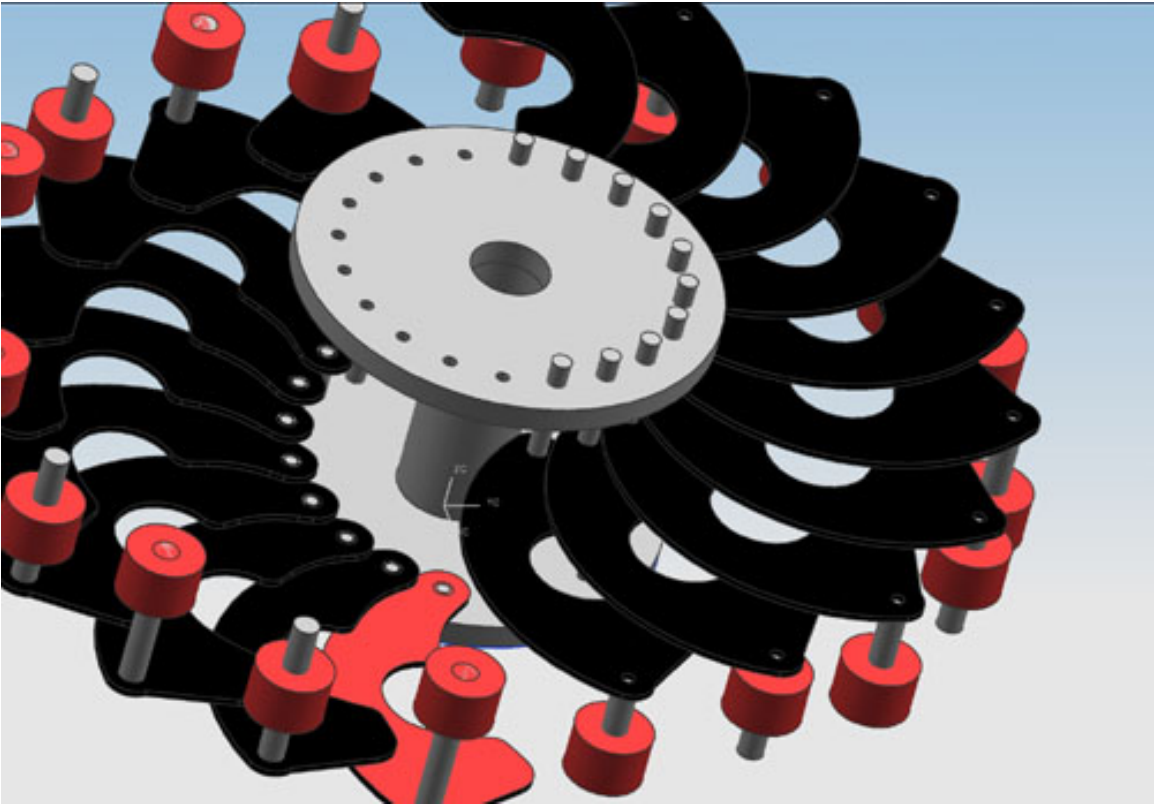
Figure 36: Design 2, isometric view, fully open.
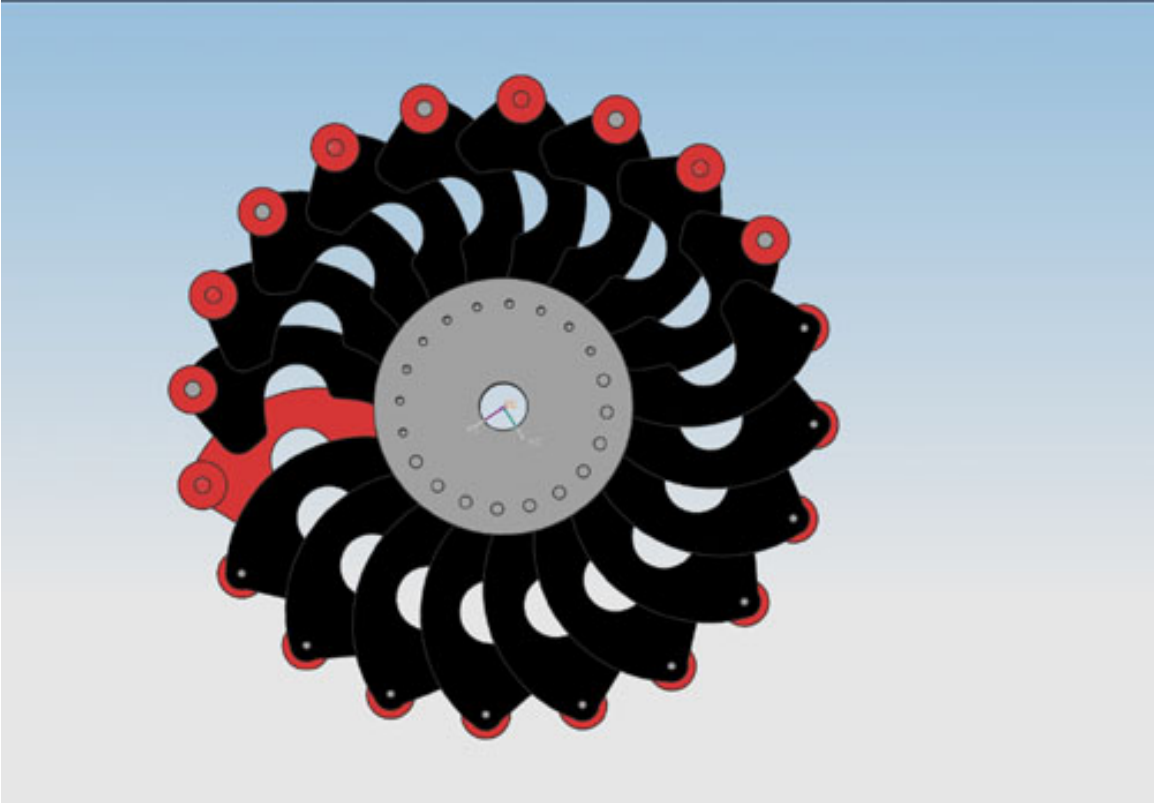
Figure 37: Design 2, top view, fully open.

In light of events, GTI rescoped the project to address 10" to 16" pipes and redesigned the device to accommodate the larger pipe sizes. The diameter of the new module measured 8" in its closed state. The number of sensors was increased to 48. They consisted of two rings of 24 and nest in their closed state.

Since the required expansion ratio was smaller, making use of the entire radius was no longer necessary and so the arm design was made simpler. The arms used for this design were all identical and machined from a flat plate. Figure 38 shows the design in it's closed state.
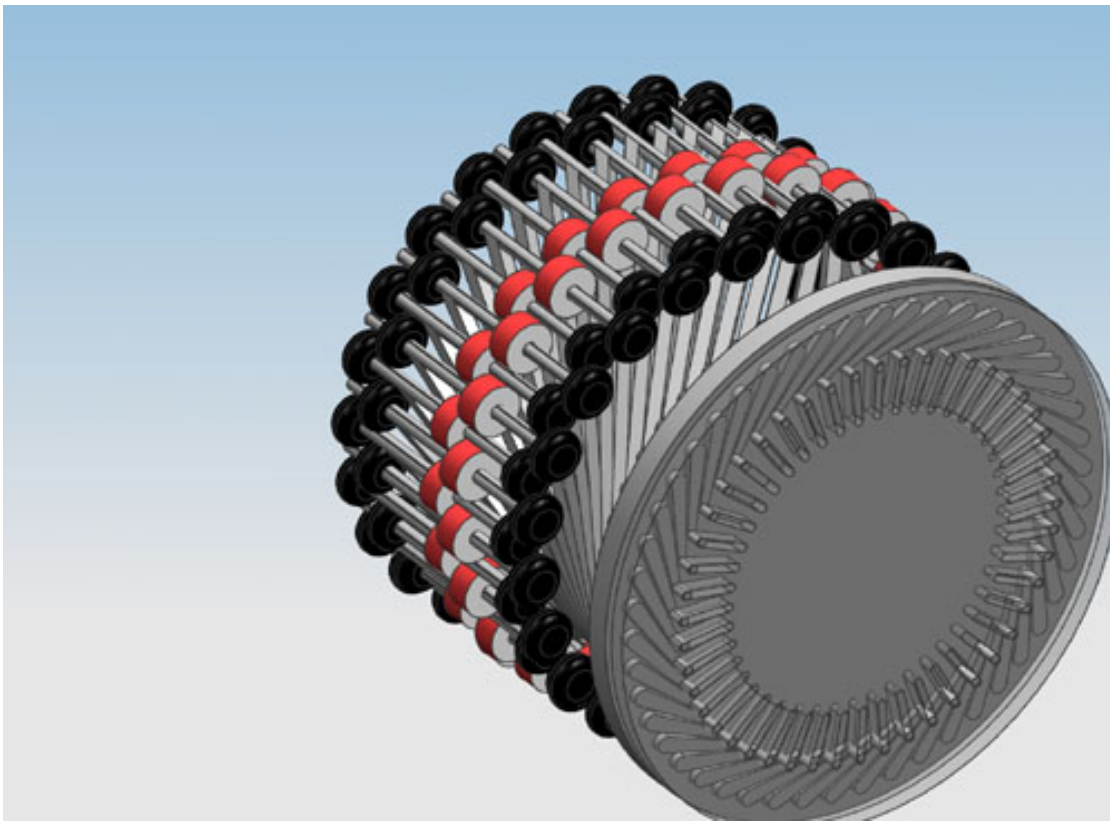
Figure 38: Final Design, isometric view, closed.

Forty-eight radial slots were machined out of an end plate. The slits allow the pinned end of a crank arm to slide. The crank arm serves as a connecting rod between the arms and the plates allowing the rotation of the plate to open the arms simultaneously. Figure 39 shows the device as the plate has been turned. The pins have traveled half the length of the slot. In Figure 40, the pins have traveled to length of the slot and are on the return as the arms are opened to their maximum position.
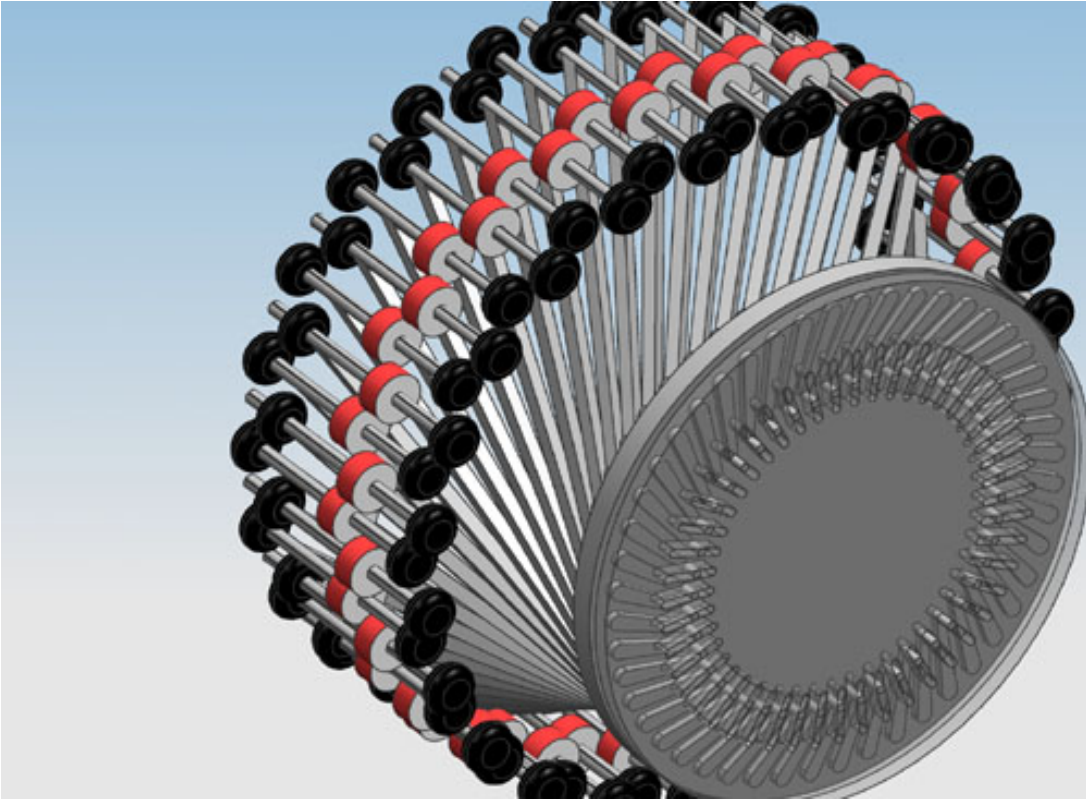
Figure 39: Final Design, isometric view, partially open.
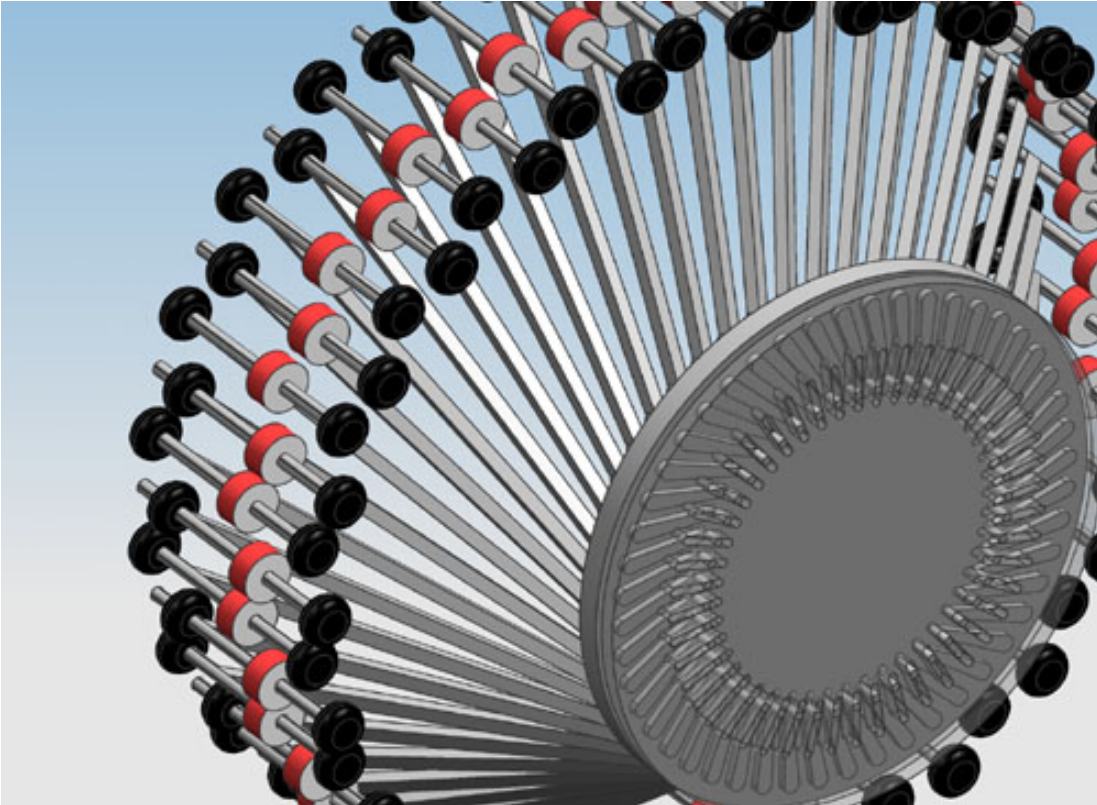
Figure 40: Final Design, isometric view, fully open.

PROTOTYPE

GTI built a prototype from the 10" to 16" design plans. The arms were water-jetted from spring steel to add some compliance. All the arms are identical and have holes to pin the sensors into place. The sensor placement is alternated from arm to arm so that they will nest with each other upon the arm assembly closing. After the sensors are mounted, wheels are attached as shown in Figure 41. The wheels serve to keep the sensors at a set location from the pipewall and prevent damage to the sensors by the pipewall. The design of the arm provides some protection for wiring between the sensor and the microprocessors. The wires would most likely be epoxied to the underside of the arm as depicted in the figure below.
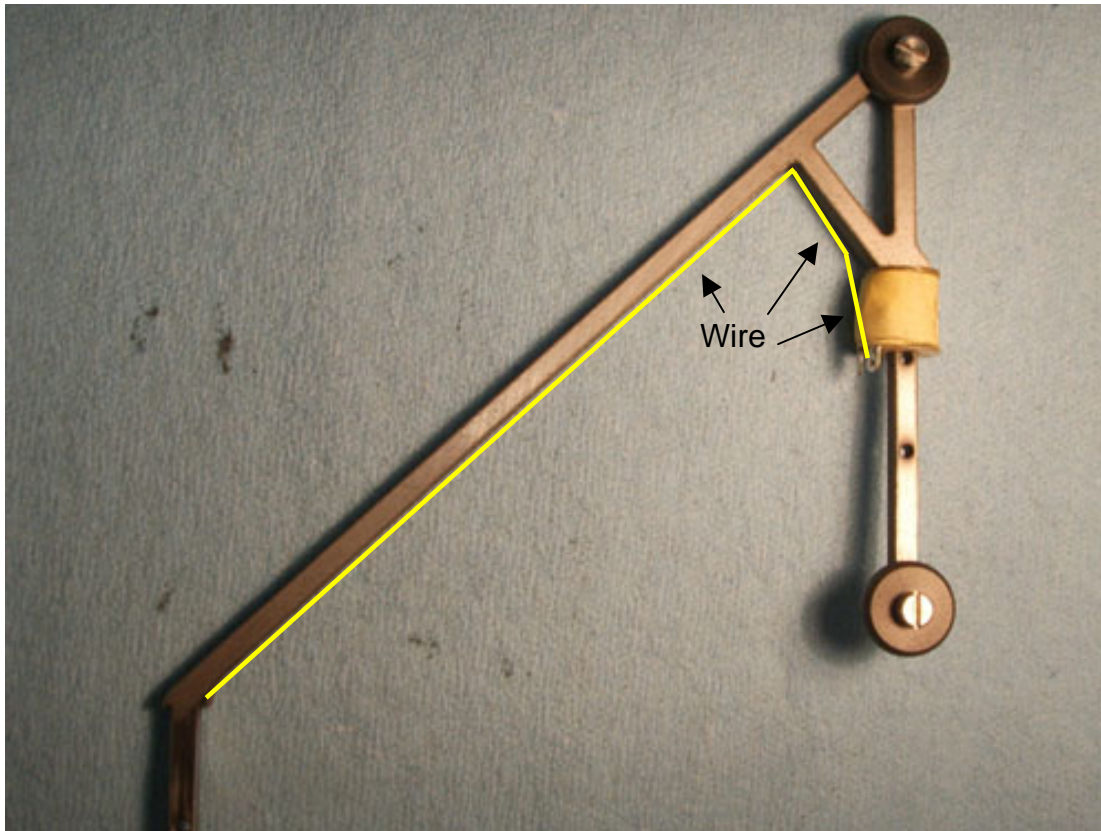
Figure 41: Single arm with coil.

The square end of the arm is rotated in a bronze bushing to minimize rotational friction during expansion and contraction. The bushings can be seen in Figure 42. They are mounted in the base plate. Also mounted to the base plate is the drive plate which contains slots for the connecting rods to rotate the arms.

There is a ring mounted to the drive plate. The drive plate is allowed to rotate approximately 35° and is contained by bushings in slots on the ring.
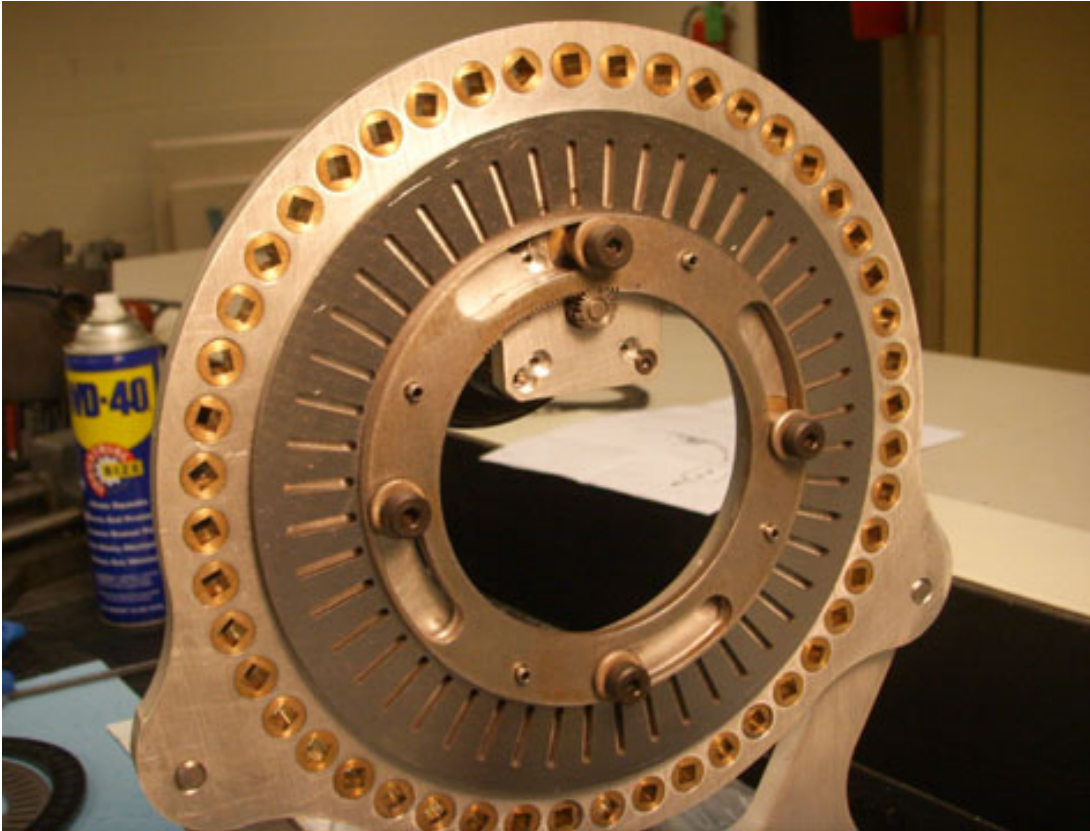
Figure 42: Base plate, pre-mounting.

Motion is accomplished by gearing. The ring has teeth machined into the inside diameter. The motor and the gear mounted to it are shown in Figure 42 at the top, center position. When the gear turns, it drives the ring and drive plate. The drive plate's motion causes the pins on the crank arm to travel which causes the arms to turn.

Figure 43 shows the module after the arms have been installed. Only one coil was mounted. The module is shown in its closed position. The diameter of the module is 7 – ¾" allowing it to pass through an 8" entrance.

Figure 44 shows the module as the arms have opened part of the way. Note the amount of travel of the arm with the sensor.

Figure 43: Module, top view, closed.

Figure 44: Module, top view, partially open.

Figure 45: Module, isometric view, fully open.

As shown in Figure 45, the diameter of the module is greater than 16" at its fully open state. The coils are aligned axially to the pipe and are equally spaced.

ELECTRONIC DESIGN AND IMPLIMENTATION

The data collection and electronics are controlled by a master PIC16F87 microprocessor that provides the magic sinewave data used to generate the drive coil signal and the slave PIC16C773 microprocessors that convert the output of the sensor amplifiers to a digital value and store it in 24LC256 256KB memory chips.

The block diagram is shown in Figure 46. The master generates the magic sinewave sequences and outputs them to the $S^\uparrow$ and $S^\downarrow$ pins. One op amp inverts the $S^\downarrow$ signal, while a second integrates the summed bit streams and outputs the resulting sine wave to a potentiometer. An inverting op amp and a non-inverting op amp amplify the sine wave and drive the exciter coil that generates the RFEC electromagnetic waves. High gain, low noise, op amps amplify the output from the sensing coils, located about 2 pipe diameters from the drive coil, and input the signal to the 12 bit ADCs of the slave microprocessors. The output of each ADC is stored in a 256 KB memory chip and can also be transmitted to an RS232 interface for monitoring by the operator at the end of the tether. The master processor can also be controlled and reprogrammed through this interface.

Information on magic sinewaves can be found on the internet, http://www.tinaja.com/magsn01.asp . They consist of carefully selected sequences of ones and zeros, easily generated by a microprocessor that can then be integrated to generate sine waves with an arbitrary number of lower harmonics forced precisely to zero.

Digital lock-in amplifiers, programmed into the slave processors, are used to filter the input signals from the sensors. The method basically consists of summing the amplified sensor signals into In-Phase and Quadrature-Phase bins for a programmable number of cycles. Figure 47 shows the frequency response to sine waves from 17.5 Hz to about 40 Hz for a digital lock-in with a 35 HZ lock frequency integrated over 10 cycles.
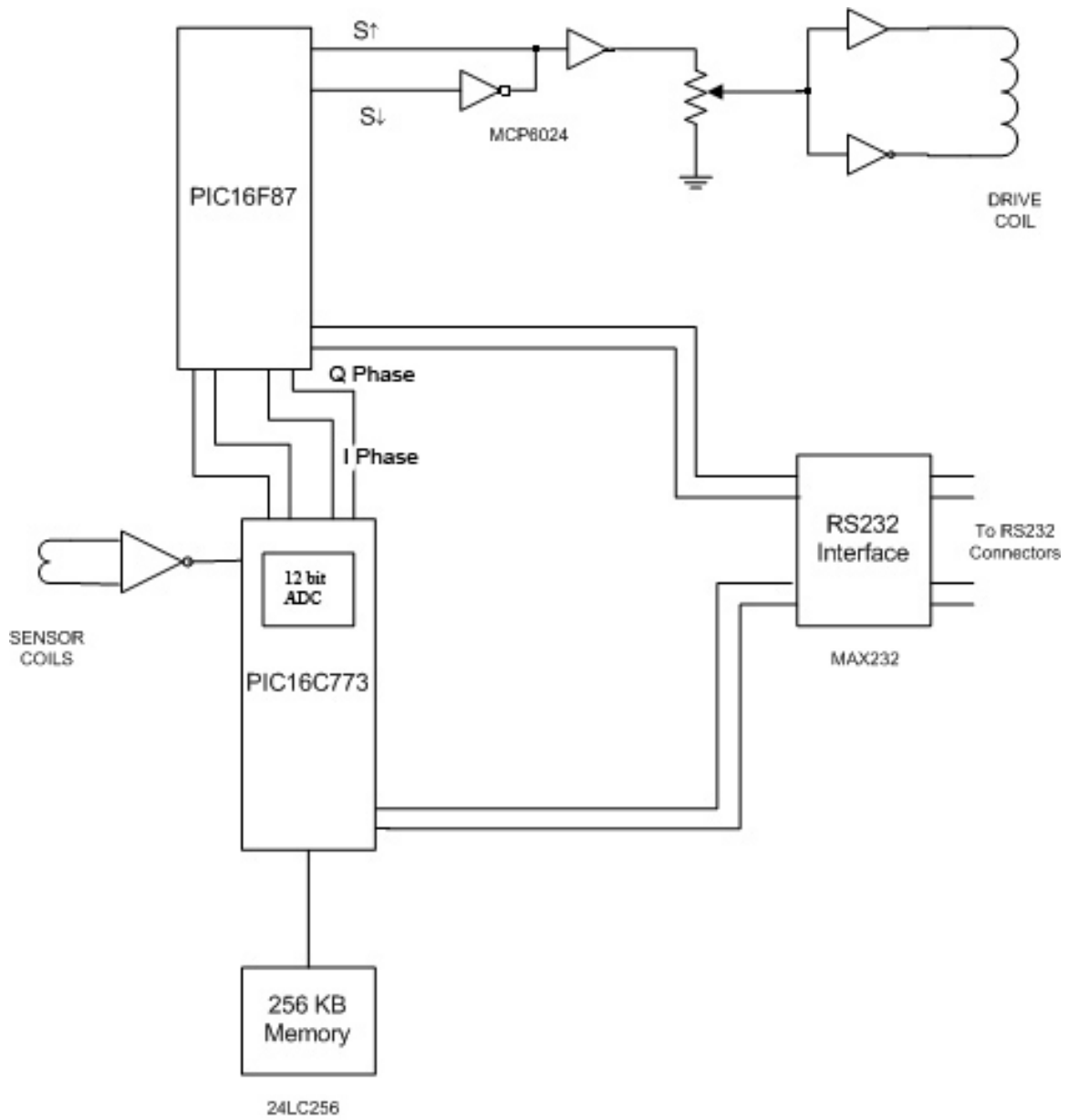
Figure 46: Block diagram of the electronic components.
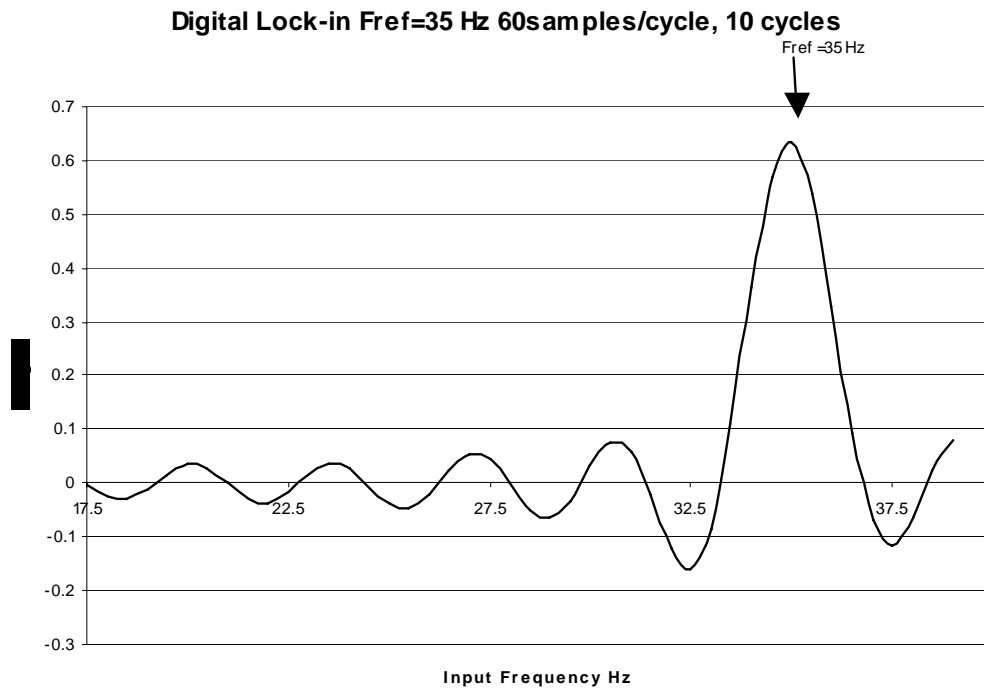
Figure 47: Digital lock-in response as a function of frequency: the lock frequency was 35 HZ.

The master microprocessor and one slave processor were assembled and tested in the seamless 6" pipe with previously manufactured drive and sensor coils. Early results showed unacceptable noise that was traced to too much vibration of the sensing coils and too wide a bandwidth for the sensor signals. The system was modified to reduce mechanical vibrations. One of the better results is shown in Figure 48. The signal from a large ferromagnetic mass is easy to see. Also visible are signals from much smaller defects (see earlier sections of this report) machined into the seamless pipe. The noise is still larger than preferable, but further mechanical improvements and better filtering should reduce noise levels to where the defect signals stand out as clearly as obtained with standard laboratory equipment.
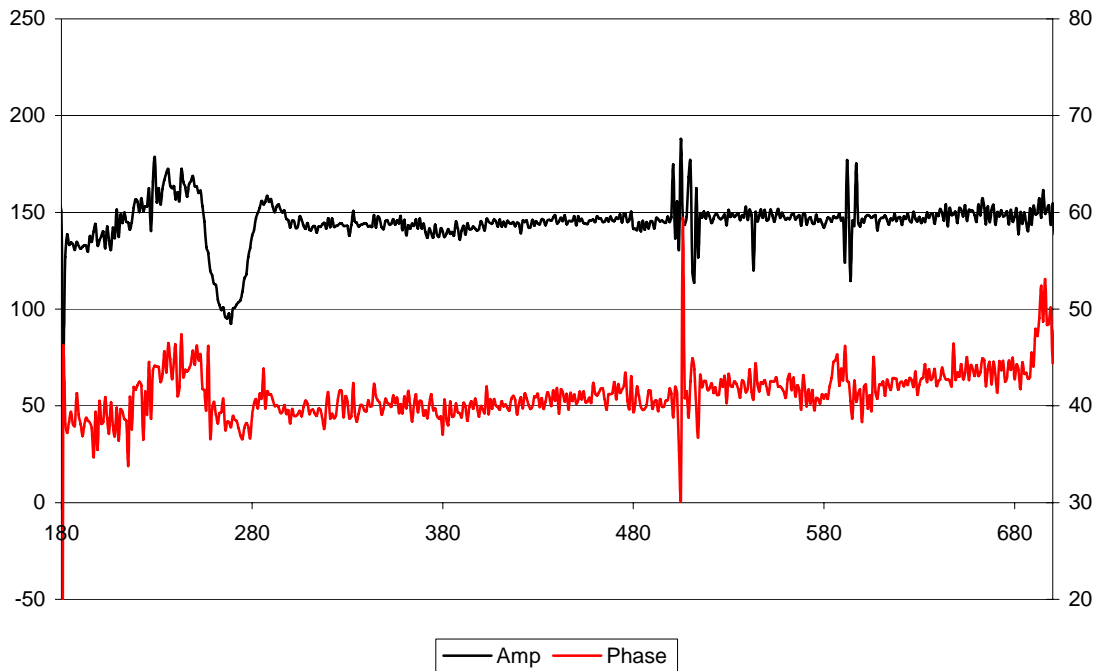
Figure 48: A test run of the electronic assembly using a master and one slave microprocessor programmed with a digital lock-in amplifier.

The electronic design for 10" to 16" pipe calls for collecting the information from 48 or more sensors. The existing electronics contains only one slave microprocessor, while the present design calls for one slave processor per coil. For the data to be available real time to the operator of the RFEC inspection unit, the results of all 48 processors need to be sent along the tether. This requires some form of multiplexing. Several schemes are under consideration. These involve one or more master processors to manage the memories and transmit the data to the operator. For example, the memory chip selected can has 8 addresses. To address all 48 channels would therefore require 6 groups of 8 each with its own PIC. An alternative scheme would dump all the data to an SD card that could then be read by the operator's PC. A final decision has not been made and implementation will require additional resources.

CONCLUSION

Although we are disappointed that the ultimate objective of this project was not reached, at this time, due to issues related to funding, we are still pleased with the quality of research that was accomplished. Improvements in the laboratory setup which include automation of the equipment, allowed us to perform a large variety of tests. We tested seven exciter coils and gained valuable knowledge about coil geometry's effect on the magnitude of the electromagnetic field. We were able to improve the sensitivity of the sensor coils and detect 5% wt defects, all the while requiring less power than would be available on an autonomous robot. We also tested commercial electronics from Russell Technologies and built and tested our own electronics.

Multiple preliminary module designs were drafted using 3D modeling software. One of these designs evolved into a final design that is currently under review for patent. This innovative design was capable of traversing pipe in two directions. With the decision to not integrate GTI's sensors with a robot, the design was resized for 10" to 16" pipe diameters, targeted for tethered platforms, and was built.

REFERENCES

W.R. McLean, W. R., US Patent 2,573,799, "Apparatus for Magnetically Measuring Thickness of Ferrous Pipe", Nov. 6, 1951

Schmidt, T. R., "The Casing Instrument Tool-…", Corrosion, pp 81-85, July 1961

Atherton, D. L., US patent 6,127,823, "Electromagnetic Method for Non-Destructive Testing of Prestressed Concrete Pipes for Broken Prestressed Wires", Oct. 3, 2000

Takach, S. F., Teitsma, A., Maupin, J., Seger, P., and Shuttleworth, P. "Remote Field Eddy Current Inspection for Unpiggable Pipelines" Proc. Of Natural Gas Technologies 2005, GTI-04/0252, Gas Technology Institute, 2005

Maupin J., Teitsma, A., "Delivery Reliability for Natural Gas -- Inspection Technologies Phase I Topical Report" October 2005

Teitsma, A., et al. "Small Diameter Remote Field Eddy Current Inspection of Unpiggable Pipelines" Journal of Pressure Vessel Technology, 2005

TABLE OF FIGURES

LIST OF ACRONYMS AND ABBREVIATIONS

RFEC	Remote Field Eddy Current
GTI	Gas Technology Institute
BOP	Bipolar Operational Amplifier
V rms	Volts root mean square
A rms	Amps root mean square
mV	Millivolt
W	Watt
UML	Unified Modeling Language
MFL	Magnetic Flux Leakage
DOE	Department of Energy
NETL	National Energy Technology Laboratory
wt	Wall Thickness
Hz	Hertz
CMU	Carnegie Mellon University